Scaling of wetted-transom resistance for improved full-scale ship performance predictions

Ocean Engineering 266 (2022) 112590

Contents lists available at ScienceDirect

Ocean Engineering

journal homepage: www.elsevier.com/locate/oceaneng

Scaling of wetted-transom resistance for improved full-scale ship performance predictions

Kadir Burak Korkmaz [a,b,*], Sofia Werner [a], Rickard Bensow [b]

[a] SSPA SWEDEN AB, Chalmers Tvärgata 10, Box 24001 Se-400 22, Göteborg, Sweden
[b] Chalmers University of Technology, Sweden

ARTICLE INFO

Keywords:
Ship resistance
Form factor
CFD
Combined CFD/EFD methods
Transom flow
Wetted-transom

ABSTRACT

Determining a ship's propulsive power is a critical stage in the design phase in which the evaluation of the stern plays a crucial role. Different flow regimes can be observed depending on the position and shape of the transom. This paper investigates the wetted-transom flow characteristics and their implications on the 1978 ITTC Performance Prediction Method. In the case of flow separation, such as the wetted-transom flow, the current ITTC-78 procedure does not provide an alternative method. Therefore, two alternative methods were proposed based on the investigations of CFD computations on seven hull forms. The firstly proposed method is a combined EFD&CFD method called the two form factor method. It requires CFD computations in model and full-scale, and it can handle any case of flow separation, including the wetted-transom flow. The second proposed method is an empirical correction formula for the hulls with a wetted-transom flow. Finally, the full-scale speed-power relations between the speed trials and the full-scale predictions from the two alternative methods and the standard ITTC-78 method were presented. It is observed that the two suggested methods considerably improve the correlation between the predictions and the speed trials.

1. Introduction

Predicting a ship's power requirement at the design stage is critical for a successful design. Meanwhile, as the ship design progresses from the initial phases to the end, the required confidence level for the speed-power prediction increases. Therefore, the speed attained at a specific power consumption needs to be verified by the most accurate prediction method for the final design. This need arises not only because of the contractual agreement on the speed-power performance of a new ship between the yard and the ship owner but also due to the legal requirements posed by the International Maritime Organisation (IMO). To reduce greenhouse gas emissions from shipping, the IMO (2011) introduced the Energy Efficiency Design Index (EEDI). The regulations require the speed-power relation of a ship to be determined through model tests. However, the model testing and the extrapolation methods used for predicting the speed-power relations face challenges for ships with substantially submerged transoms. Considering that the EEDI calculations are performed at the scantling draught, where the transoms of many vessels are submerged, it is significant to improve the accuracy and reliability of the EEDI values further.

Nearly all modern cargo vessels have a transom stern. The flow regime behind the transom can be characterised under three main categories as suggested by Larsson and Raven (2010): regular, dry-transom, and wetted-transom flow. In the case of a regular transom flow, the lower edge of the transom is above the still water level, and the waves leave the hull smoothly, similar to a cruiser stern design. The dry-transom flow indicates the free-surface, and the flow smoothly leaves the transom edge tangential to the buttocks. The criterion for dry-transom flow occurrence is that the pressure at the edge of the transom must be equal to the atmospheric pressure (Larsson and Raven, 2010). Increasing the transom submergence of a vessel or decreasing the speed will increase the required hydrodynamic pressure to sustain the dry-transom flow. As a result, the upward curvature of the streamlines of the flow behind the transom will increase. The increased steepness of the streamlines and the momentum deficit of the flow leaving the hull due to the boundary layer will cause the longitudinal velocity to disappear at a certain point and leads to the emergence of a spilling wave breakers between the transom and the first wave crest (Starke et al., 2007). Increasing the transom submergence or decreasing the speed further will lead the spilling breaker to reach the transom. As a result, a recirculation region emerges and gives rise to the wetted-transom flow, which is the main subject of this paper.

The transom stern submergence can vary significantly depending on the ship type and operational profile. Some full block vessels, such as

* Corresponding author at: Chalmers University of Technology, Sweden.
E-mail addresses: burak.korkmaz@sspa.se, korkmaz@chalmers.se (K.B. Korkmaz).

https://doi.org/10.1016/j.oceaneng.2022.112590
Received 22 June 2022; Received in revised form 7 September 2022; Accepted 13 September 2022
Available online 30 September 2022

tankers and bulk carriers, and some low block fast vessels, often feature submerged transoms at rest for design and scantling draughts. The full block vessels operate at low Froude numbers; hence, obtaining a dry-transom flow is difficult due to the thick boundary layer, substantial transom submergence, and low speeds. The wetted-transom flow can be observed for some ships even though the low block vessels such as Ro-Ro, Ro-Pax, and PCTCs are designed to operate with a dry-transom. These vessels may have substantially large submerged transoms due to the loading condition of the ship (a significant aft trim) combined with speeds lower than the design speed that may result in wetted-transom flow.

The towing tank testing and extrapolation procedures have been used since the 19th century to predict the performance of a ship in deep and calm water. The International Towing Tank Committee (ITTC) put forward a towing tank testing and extrapolation procedure denoted as 1978 ITTC Performance Prediction Method (ITTC, 2021a) as a result of decades-long developments and discussions. One of the main pillars of this procedure is the form factor concept (Hughes, 1954) used for scaling the viscous resistance from model to full-scale. As explained in Section 2, the form factor approach is invalid when there is a flow separation in the boundary layer surrounding the hull. However, flow separation can occur in different ways for a vessel. Hence, it is essential to differentiate the mechanisms and causes of flow separations observed at flows around ships.

The first common type of flow separation is the bubble type (Larsson and Raven, 2010) which may be present at the stern of full block vessels. The bubble type separation is often a result of a sudden increase of pressure after passing a low-pressure region such as the bilge region. The distinct feature of this type of separation is that it results from an interaction between the boundary layer and the pressure distribution. The pressure distribution around the hull is the main driver of the boundary layer development. However, the pressure also is influenced by the boundary layer due to the displacement effect. Due to this relation, the bubble type separation often disappears with the increasing Reynolds number (Re) as presented in Korkmaz et al. (2021). Increasing Re reduces the viscosity effects and eases the adverse pressure. As a result, the flow separation dissipates, reducing the form factor.

The second type of flow separation is the recirculation flow region behind a substantially submerged transom, similar to a flow through a backward-facing step. The mean velocities around the stern overhang of a vessel are subjected to the sudden increase of cross-sectional area, causing the flow separation, as the mean velocities cannot follow the sharp turn. As a result, a low-pressure region is formed behind the transom, and the water surface is lower than the surrounding water levels. If the vessel speed increases or the transom submergence decreases, the water surface reaches the transom edge, and eventually, the transom becomes dry again, and the flow separation disappears. It is noteworthy to emphasise that flow separation behind the transom differs from the bubble type separation since the boundary layer effects and the pressure gradient are not the root causes of a largely submerged transom. Therefore, the full-block vessels with substantial transom submergence are most likely to experience wetted-transom (separated flow) both in model and full-scale. However, extra caution is needed for the vessels with a partially wetted-transom (coexisting smooth free-surface and significant spill breakers) as scale effects may result in different flow regimes in model and full-scale (Starke et al., 2007).

The wetted transom flows do pose issues with the 1978 ITTC Performance Prediction Method due to the separated and turbulent flow behind the transom, where a substantial amount of water is trailing the hull rather than the surrounding flow. This issue is reported by the ITTC (2021e) for the form factor derivation method as "it should be noted that Prohaska's method should not be used for any vessel with substantial transom sterns for which the transom runs wet at the speed range for the Prohaska test". However, no alternative method is suggested by the ITTC. One towing tank institution is known to employ an empirical correction for the transom submergence in their extrapolation procedure; however, neither the derivation nor the demonstration of this correction is open in the literature. Several studies (Farkas et al., 2018; Islam and Guedes Soares, 2019) investigated the hydrodynamic characteristics of full-scale ships at different draughts and trim conditions; however, no recommendations were provided for the issues caused by the wetted-transom flow. Given the importance of accurate methods for speed power predictions for EEDI and contracts, an alternative method or a correction procedure is needed for the vessels with substantial transom submergence. Due to the extreme scarcity of sea trial data carried out at scantling draught, it is difficult for towing tanks to derive correlation factors that account for these effects. Therefore, this paper aims to

- explain the wetted-transom flow characteristics in model and full-scale,
- highlight the issues with the 1978 ITTC Performance Prediction Method when flow separation exists
- quantify the resistance caused by the wetted-transom
- propose an alternative combined EFD/CFD method which can handle flow separations in the extrapolation process
- propose an empirical correction formula that can be integrated into the existing ITTC-78 method without the need for CFD computations.

This paper is structured as follows: Section 2 briefly describes the standard extrapolation of the towing tank resistance measurements from model to full-scale. The resistance extrapolations with and without a flow separation caused by a wetted-transom flow are illustrated. Additionally, an alternative method denoted as two form factor is suggested in Section 2. The geometrical features and parameters for a submerged transom are defined in Section 3. The numerical set-up used for the investigation of the transom flow is described in Section 4. The computational conditions and the test cases used in this study are presented in Section 5. In Section 6, a grid dependency study (Section 6.1), a qualitative (Section 6.2) and quantitative analysis (Section 6.3) of the flow behind the transom in model and full-scale are presented. Section 7 introduces an alternative empirical method for extrapolation of a towing tank test to full-scale resistance. The comparison of speed trials to the different prediction methods is presented in Section 7.1. Finally, the conclusions are summarised in Section 8.

2. Extrapolation of resistance from model tests to full scale, and the two form factor method ($2-k$ method)

2.1. Standard ITTC-78 method

In this study, the procedure recommended by ITTC (2021a) is used to extrapolate the towing tank test results to full scale. According to the 1978 ITTC Performance Prediction Method, the total resistance coefficient of the full-scale ship is calculated as

$$C_{TS} = (1+k)C_{FS} + \Delta C_F + C_A + C_R + C_{AAS}, \quad (1)$$

where k is the form factor, C_{FS} is the frictional resistance coefficient in full scale (the subscript 'S' signifies the full-scale ship), C_R is the residual resistance coefficient, ΔC_F represents the roughness allowance, C_A is the correlation allowance, and C_{AAS} is the air resistance coefficient.

According to the recommended procedure of ITTC (2021e), the form factor is obtained by the Prohaska method (Prohaska, 1966) in the model scale. Additionally, the determination can be supported by CFD calculations according to ITTC (2021b) following the procedures described in ITTC (2021c). The residual resistance, which is assumed to be the same in model and full-scale, is then obtained as

$$C_R = C_{TM} - (1+k)C_{FM}, \quad (2)$$

where C_{TM} is the total resistance coefficient (the subscript 'M' signifies the model scale). C_{TM} is measured at each speed in the towing tank,

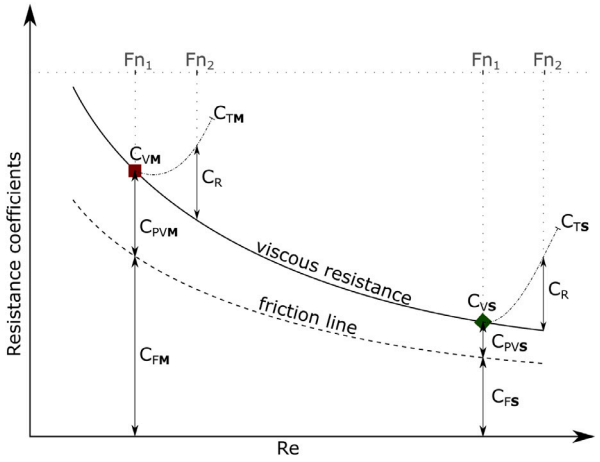

Fig. 1. The form factor hypothesis.

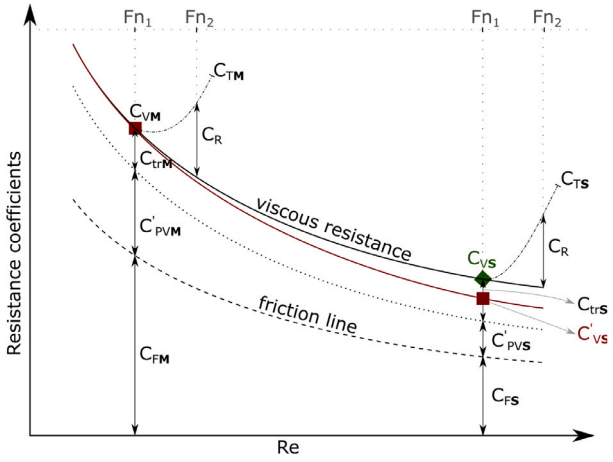

Fig. 2. Extrapolation method with a deeply submerged transom. (For interpretation of the references to colour in this figure legend, the reader is referred to the web version of this article.)

and C_{FM} is obtained from the friction lines. In this study, the Prohaska and CFD based form factor determination methods were used for the form factor derivations as described in ITTC (2021e). The latter method follows the assumptions of Hughes (1954) and is derived using the relation:

$$(1+k) = \frac{C_F + C_{PV}}{C_{FM}} = \frac{C_V}{C_{FM}}, \tag{3}$$

where the frictional resistance coefficient (C_F) and viscous pressure coefficient (C_{PV}) are obtained by the double-body CFD simulation. C_{FM} in the denominator of Eq. (3) is the equivalent flat plate resistance in two-dimensional flow obtained from the same Reynolds number as the computations. When the CFD based form factor determination is used, C_{FM} in Eq. (3), C_{FM} in Eq. (2) and C_{FS} in Eq. (1) are derived from the same friction line.

In this study, the frictional resistance coefficients, C_{FM} and C_{FS}, are obtained by using three different friction lines: the ITTC-57 model-ship correlation line (ITTC, 1957), and two numerical friction lines for EASM and k−ω SST turbulence models, respectively, proposed by Korkmaz et al. (2019b).

The validity of the form factor approach and the ITTC-78 extrapolation method shown in Eq. (1) is based on several criteria stated in Hughes (1954),

- the C_{PV} is proportional to the C_F when the flow is turbulent and free from separation
- the given hull is smooth and has a symmetrical form when towed at zero incidence angle.

Assuming this preconditions are fulfilled, the Eq. (1) can be visualised as in Fig. 1 excluding the roughness (ΔC_F), correlation allowance (C_A) and air resistance (C_{AAS}) terms for simplicity. To obtain the C_{TS}, model tests should be performed following the Fr similarity. Once the C_{TM} is measured and the form factor is determined, the C_R is obtained as shown in Eq. (2). As the form factor is the same at the model and full-scale, the full-scale viscous resistance is calculated as $C_{VS} = (1+k)C_{FS}$. The summation of the residual and viscous resistance for a given Fr will result in full-scale total resistance coefficient.

2.2. The two form factor method

In the case of a vessel with a deeply submerged transom for which the transom runs wet, the form factor approach as described in ITTC (2021e) is destined to fail as the wake of the transom constitutes separated flow which violates the preconditions of the form factor approach (Hughes, 1954). The recirculating flow behind the wake of the transom differs from the bubble type separation often observed around the stern bulbs of full block vessels in model scale but not in full scale. As discussed in Section 6, the recirculating flow behind the transom is persistent through the model scale to the full-scale Reynolds numbers. As a result of this persistent recirculating flow, using the same form factor in model and full-scale will result in an under-prediction of the full-scale viscous resistance. In Fig. 2, this is illustrated by decomposing the viscous resistance coefficient, C_{PVM}, which is the form resistance as described in Hughes (1954),

$$C_{PVM} = C'_{PVM} + C_{trM}, \tag{4}$$

where C'_{PVM} is the part that is proportional to the frictional resistance coefficient of a friction line, and the flow behind the wet transom is the cause of C_{trM}. Note that C_{trM} is the part that is *not* proportional to the C_F. As argued later in Section 6, the size of the C_{trM} remains approximately the same in model and full-scale Reynolds numbers. Hence, using the same form factor in model and full-scale implies that both C'_{PVM} and C_{trM} scales down proportional to the C_F as visualised as the continuous red line in Fig. 2. Therefore, the viscous resistance scaling as Eq. (1) has to be either corrected or predicted directly by CFD for the vessels with a wetted transom flow. The latter method is referred to as the two form factor method or $2-k$ *method* throughout the paper. The authors demonstrated earlier in Korkmaz et al. (2021) that the two form factor method is helpful for hulls with mild flow separation at the stern (bubble type). This paper employs the same technique on the substantially submerged transoms. The $2-k$ *method* is applied by the following steps:

1. C_{TM} is obtained from the towing tank tests.
2. The model-scale form factor, k_M is determined either by the Prohaska method (Prohaska, 1966) or by CFD (Korkmaz et al., 2021).
3. The residual resistance is calculated as $C_R = C_{TM} - (1+k_M)C_{FM}$
4. The full-scale form factor, k_S, is calculated using CFD based form factor method
5. The full-scale total resistance coefficient is calculated as

$$C_{TS} = (1+k_S)C_{FS} + \Delta C_F + C_A + C_R + C_{AAS}\ , \tag{5}$$

where,

- Residual resistance is obtained by using the model-scale form factor
- Viscous resistance is obtained by using the full-scale form factor.

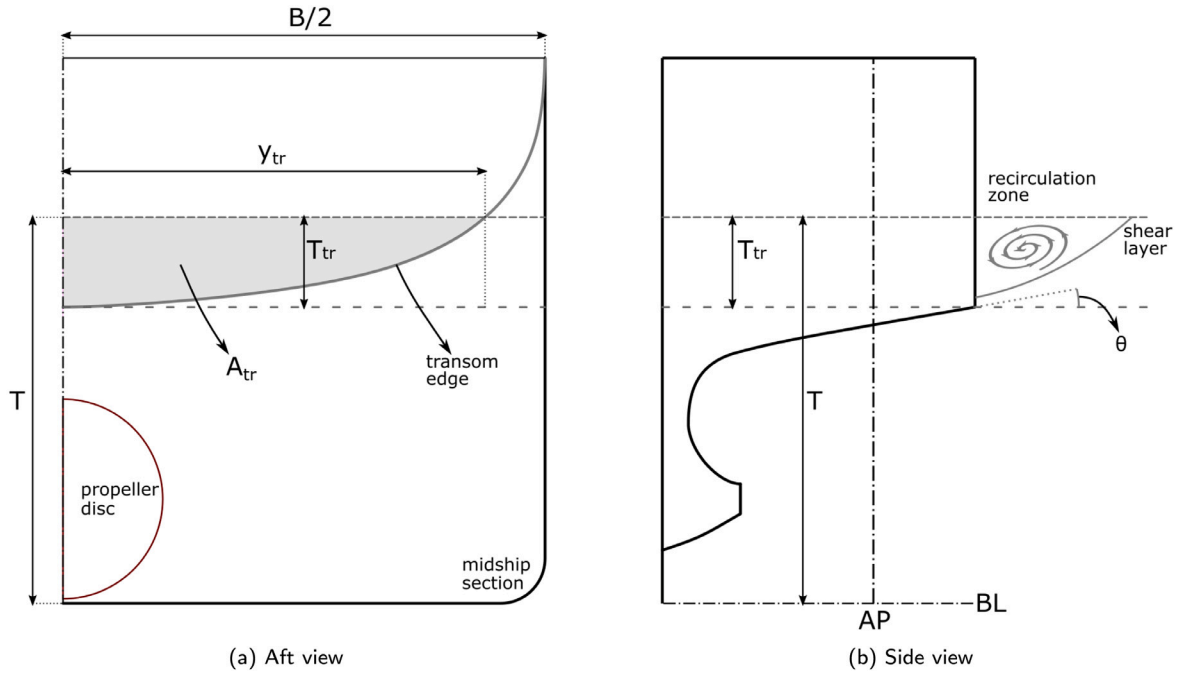

Fig. 3. Geometrical descriptions of a submerged transom.

As an alternative to the $2-k$ method, a correction method is suggested in Section 7. This correction aims to counterpoise the viscous resistance deficit in the case of a wetted-transom when the standard ITTC-78 method (ITTC, 2021a) is used, as illustrated in Fig. 2.

3. Terms and definitions for a submerged transom

Several parameters are defined to describe the transom flow, and a submerged transom is illustrated in Fig. 3. The draught and beam of the vessel are signified as T and B, respectively. The submerged part of the transom is indicated with light grey shading in Fig. 3(a), and the area of the submerged transom is presented as A_{tr}. Between the undisturbed water surface to the bottom-most part of the transom is indicated as the transom submergence, T_{tr}. The intersection point between the transom edge (light grey solid line) and the water surface is horizontally measured by the maximum width of the transom, y_{tr}. The last geometrical feature is the slope of the stem profile near the transom, θ, as shown in Fig. 3(b). The parameters related to waterline shapes or angles are disregarded as the flow around the stern rarely follows the waterlines; instead, the buttocks (or diagonals) represent the flow better.

For the submerged transom cases, the transom Froude number (Saunders, 1957),

$$Fr_{tr} = \frac{V}{\sqrt{gT_{tr}}}, \tag{6}$$

is a significant parameter that may indicate (even though with little validity) what flow type occurs behind the transom as indicated by Larsson and Raven (2010).

Two parameters are derived from the submerged transom area. The first parameter is the ratio between the A_{tr} and the maximum cross-section area, A_{max}. This area ratio is defined as:

$$tr_{ratio} = A_{tr}/A_{max} \ . \tag{7}$$

The other parameter indicates how full is the transom edge section. Observing this parameter may help to distinguish the effects caused by V-shaped or U-shaped shaped sections. The fullness of the transom is measured as:

$$tr_{fullness} = A_{tr}/(2y_{tr}T_{tr}) \ . \tag{8}$$

4. Flow solver, grid generation, computational domain, and boundary conditions

The XCHAP module of SHIPFLOW version 6.6 is used for solving the steady-state viscous flow (Broberg et al., 2014). The finite volume method is utilised to solve Reynolds Averaged Navier–Stokes (RANS) equations. The discretisation of the convective terms is achieved by the first order accurate Roe scheme, and an explicit flux correction is applied to increase the order of accuracy. Two turbulence models are available in the XCHAP solver: explicit algebraic stress model (EASM) as described by Deng and Visonneau (1996) and $k-\omega$ SST as described by Menter (1994). In this study, both turbulence models are used.

The viscous flow solver XCHAP accepts only structured grids, which can be in H-H, H-O, or O-O topologies. The grid generator of SHIPFLOW, XGRID, is used for the study to generate all the grids. The parametrised nature of grid generation with XGRID makes it possible to generate almost identical grid distribution in the longitudinal and circumferential directions for most of the conventional hulls simulated. However, the grid distribution in the normal to the hull surface can vary for each hull since the Reynolds number differs. As a result, different first cell sizes in the normal direction to the wall and cell growth ratios are obtained to achieve (approximately) the same y^+ values.

The CFD computations for the form factor calculations in this study were performed as double-body (DB) RANS computations with rudders integrated into the flow domain with an overlapping grid technique (Regnström, 2008). In addition, for a limited number of cases, free-surface (FS) RANS computations were also performed using the XCHAP solver to investigate the flow around the transom region. Detailed information about the free-surface treatment and the solver for the FS RANS method is explained by Orych and Larsson (2015).

The computational domain is shaped as a quarter of a cylinder. The distance between inlet and fore-perpendicular (FP) is $2.0L_{PP}$, outlet plane is located at $1.0L_{PP}$ behind the aft-perpendicular, and the radius of the cylindrical outer boundary is $3L_{PP}$.

Boundary types employed in XCHAP are no-slip, slip, inflow, outflow, and interior. The Inlet boundary condition sets a fixed uniform velocity (U_∞), a zero pressure gradient normal to the inlet boundary,

and the estimated turbulent quantities. The turbulence quantities, specific turbulence dissipation rate, and turbulent kinetic energy at the inlet are estimated as explained in Korkmaz et al. (2021). Outflow condition only consists of a Neumann boundary condition for velocity, turbulent kinetic energy, and pressure. As all computations were performed with half the body, the symmetry condition is used at the centre plane. The symmetry condition is similar to the slip condition where the normal velocity and normal gradient of other variables are set to zero. The no-slip condition specifies the velocity components, turbulent kinetic energy, and normal pressure component as zero at the wall, such as the hull and the rudder surfaces. The turbulence closure modelling is valid up until the no-slip wall. Therefore, computations were performed with the wall resolved approach, i.e. no wall functions.

5. Test cases and computational conditions

Seven different vessels have been investigated. Five of the test cases (referred to as H1, H2, H3, H4, and H5) are common cargo vessels which have been model tested, and four of the hulls have corresponding full-scale speed trials performed either at design or scantling loading conditions where the transoms were submerged at rest. Even though no full-scale measurement exists, the KVLCC2 and KCS hull forms are included in this study to diversify the ship types. The hull and rudder geometries were obtained from Tokyo (2015) and SIMMAN (2008) workshops for KCS and KVLCC2, respectively. The L_{PP} of the vessels are ranging from 170 m (denoted as m) to 320 m, and block coefficients (C_B) vary between 0.6 and 0.85. The Froude numbers (the achieved speed at 75% MCR except for KVLCC2 and KCS) cover the range of 0.14 to 0.2.

Two of the hull forms had one sea trial performed per vessel. The other vessels were built in series, and speed trials were performed for each sister ship. The data set consists of 10 sea trials in total. The trial measurements were conducted by the yards and analysed by SSPA with an in-house software according to ITTC Recommended Procedures and Guidelines for Preparation, Conduct and Analysis of Speed/Power Trials (ITTC, 2017b) and ISO Ships and marine technology—Guidelines for the assessment of speed and power performance by analysis of speed trial data (ISO, 2015). The sea trials conform to the ISO 15016/ITTC limits on weather conditions.

The computational conditions for each test case replicate the same conditions in the corresponding towing tank tests, such as the non-dimensional quantities, Re and Fr, loading condition, and geometrical features.

6. Results

The analysis of approximately 500 double-body and 40 free-surface RANS computations of the seven hulls under the conditions stated in Section 5 is discussed in this section.

6.1. Grid dependence study

Grid dependence studies were performed only for the H1 test case in model and full-scale to quantify the numerical uncertainties (U_{SN}). Following the best practice guidelines for the double-body computations (Korkmaz et al., 2021), geometrically similar six grids were generated. As the H1 test case is computed at the scantling draught, where the transom is deeply submerged, the flow behind the transom is likely to include a separated flow. Therefore, before the grid dependence study, the grid resolution behind the transom was investigated with the help of a grid refinement zone (Broberg et al., 2014). Unfortunately, the H1 hull form cannot be presented due to confidentiality. Instead, the KCS hull was used to visualise the generated grids as they are similar to the H1 grids. The grid density of the second-finest grid (denoted as g_2) without refinement is presented in Figs. 4 and 5 for the KCS hull at 12.85 m draught. As seen in Fig. 4, the longitudinal and circumferential grid distribution on the hull, the rudder, and the grid resolution behind the transom are shown. The grid resolutions of the hull and the rudder in the normal direction are presented in Fig. 5. The grid behind the transom is stretched towards the transom edge as the pressure and velocity gradients are expected to be high where the separation initialises. As an alternative to no refinement, a grid refinement was added to the region marked with the solid red lines in Figs. 4 and 5. After the refinement, each grid cell within the solid red lines was divided into 64 pieces, hence, heavily refining the grid behind the transom. Between the refined and non-refined grids, the computed viscous resistance differed 0.7% and 1.3% with the EASM turbulence model for the model and full-scale, respectively. Considering the additional resources spent on the added 3.3 million cells behind the transom and the small differences in the integrated forces between the two grids, the non-refined grids, shown in Figs. 4 and 5, were selected for the grid dependence study. The total number of grids and the grid refinement ratios ($h_1/h_i = \sqrt[3]{N_{grid_1}/N_{grid_i}}$) are presented in Table 1 for the six grids for model (MS) and full-scale (FS) computations.

All computations were performed in double precision to eliminate the round-off errors. The iterative uncertainties were quantified by the standard deviation of the force in percent of the average force over the last 10% of the iterations. Iterative uncertainty (U_I) for C_F, C_{PV} and C_V are presented in Table 2 for the six grids for model and full-scale computations. The maximum standard deviations for C_F, C_{PV} and C_V were kept below 0.02%, 0.51% and 0.1%, respectively. Even though a large recirculating flow follows the wake of the transom, the average U_I of geometrically similar six grids are reasonably small, and they are largely similar between the model and full-scale computations as seen in Table 2. In the light of these observations, it was assumed that the numerical errors are dominated by the discretisation errors and both iterative errors and round-off errors are neglected.

Table 1
Total number of cells, and the grid refinement ratios for the grid dependence study.

Grid	MS		FS	
	Cell count [M]	h_1/h_i	Cell count [M]	h_1/h_i
g_1	12.6	1.00	18.14	1.00
g_2	7.7	1.18	10.99	1.18
g_3	4.7	1.39	6.69	1.39
g_4	2.8	1.65	3.97	1.66
g_5	1.7	1.94	2.47	1.94
g_6	1.1	2.28	1.50	2.30

Table 2
Standard deviation of C_F, C_{PV} and C_V over the last 10% of the iterations.

U_i	Turb. model	MS		FS	
		max	mean	max	mean
C_F	EASM	0.01	0.00	0.00	0.00
	$k-\omega$ SST	0.02	0.00	0.01	0.00
C_{PV}	EASM	0.45	0.21	0.08	0.06
	$k-\omega$ SST	0.51	0.20	0.35	0.25
C_V	EASM	0.09	0.04	0.02	0.01
	$k-\omega$ SST	0.10	0.04	0.10	0.07

Table 3
Numerical uncertainty of the finest grid, g_1.

$U_G\%S_1$	Turb. model	MS	FS
C_F	EASM	1.3	1.6
	$k-\omega$ SST	0.7	1.5
C_{PV}	EASM	11.7	30.2
	$k-\omega$ SST	55.2	14.0
C_V	EASM	0.68	5.09
	$k-\omega$ SST	2.9	1.7

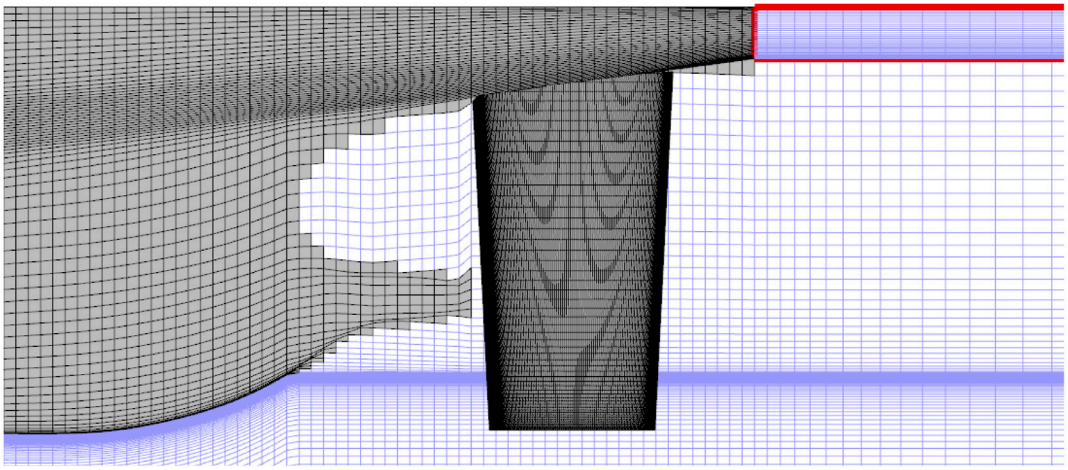

Fig. 4. Second finest grid, g_2, of KCS from side view. (For interpretation of the references to colour in this figure legend, the reader is referred to the web version of this article.)

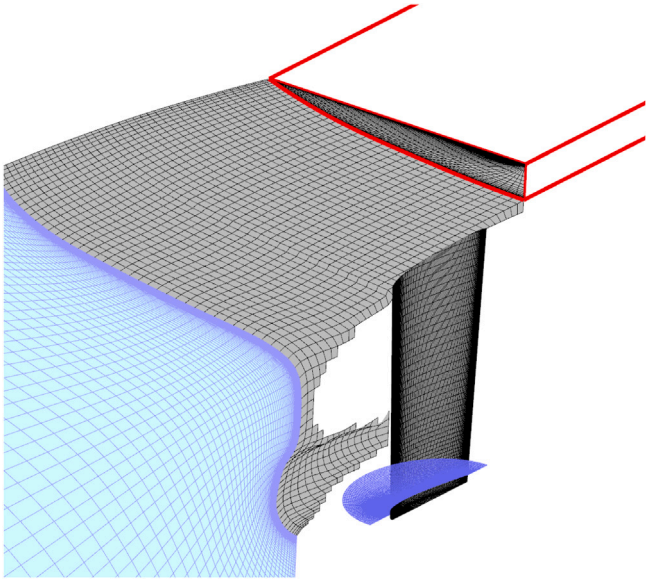

Fig. 5. Second finest grid, g_2, of KCS from aft perspective view. (For interpretation of the references to colour in this figure legend, the reader is referred to the web version of this article.)

Table 4
Numerical uncertainty of the second finest grid, g_2.

$U_G\%S_2$	Turb. model	MS	FS
C_F	EASM	2.0	2.4
	$k-\omega$ SST	1.0	2.2
C_{PV}	EASM	16.5	39.5
	$k-\omega$ SST	57.6	18.4
C_V	EASM	0.9	6.9
	$k-\omega$ SST	2.9	2.2

The procedure proposed by Eça and Hoekstra (2014) was used to predict the grid uncertainties (U_{SN}) which are presented for the finest (g_1) and the second finest (g_2) grids as a ratio of the computed value ($U_{SN}\%S_1$ and $U_{SN}\%S_2$ where S_i represents the computed value) in Tables 3 and 4, respectively. The grid uncertainties on C_F vary between 0.7 to 1.6 per cent of the computed result of S_1, while the grid uncertainty on C_{PV} varies greatly between model and full-scale and also the different turbulence models. The variation of U_G on C_V is somewhat less compared to the viscous pressure resistance. The large fluctuation in the grid uncertainties is explained by the scatter in the computed values, which strongly penalises the estimated uncertainties (Eça and Hoekstra, 2014). Computed values for C_F, C_{PV} and C_V are presented in Fig. 6 in a percentage of the result of the finest grid. The C_F and C_{PV} values in Fig. 6 shows oscillatory behaviour, which is observed significantly more for the latter. The main cause of these fluctuations can be traced back to the grid generation technique, a structured grid with a stair-step profile in the stern and stem profiles. Due to rapid curvature changes around the bulbous bow and aperture between the stern bulb and stern overhang, the structured grid captures the stern and stem profiles differently. This abrupt grid change near the sensitive regions, such as the stagnation pressure point, can lead to noticeable fluctuations, especially in the pressure resistance coefficient, as observed in Fig. 6. Another significant observation is that the grid dependency is significantly larger in full-scale computations than in the model scale. The C_V varies less than 0.5% for the four finest grids (g_1 to g_4) in model scale, while the variation of C_V in full scale is up to 2%.

The estimated numerical uncertainties are shown in Tables 3 and 4, and the fluctuations of the computed resistance coefficients are largely similar to the earlier study (Korkmaz et al., 2021) where the same code and grid generation technique was applied to different hulls and loading conditions. However, due to the drawbacks of the grid generation, the numerical uncertainties on C_{PV} are rather significant. However, its reflection on C_V is limited, and the variation on the predicted form factors is relatively small. Therefore, the grid setup of the second finest grid, g_2, has been chosen for the rest of the investigations for the other hulls. As a result, the grid cell count was reduced to approximately 7.7 and 11.0 million in model and full-scale, respectively, and computational time was shortened compared to the finest grid. Considering that over 500 computations were performed for this study, a significant computational effort was saved without sacrificing numerical uncertainty on C_V too much.

6.2. Transom stern flow

This section will investigate the transom stern flow of the test case H1 in detail. The draught of the vessel was varied in three steps. As a result, different transom submergence levels were computed in model and full-scale for EASM and k-ω SST turbulence models.

6.2.1. The effect of free-surface modelling

In order to calculate the CFD based form factors, double-body (DB) RANS computations are needed since the Eq. (3) requires the viscous resistance as the input instead of the total resistance, which can be obtained from a free-surface (FS) RANS computation. As mentioned earlier, the transom flow regime depends on not only the hull shape and

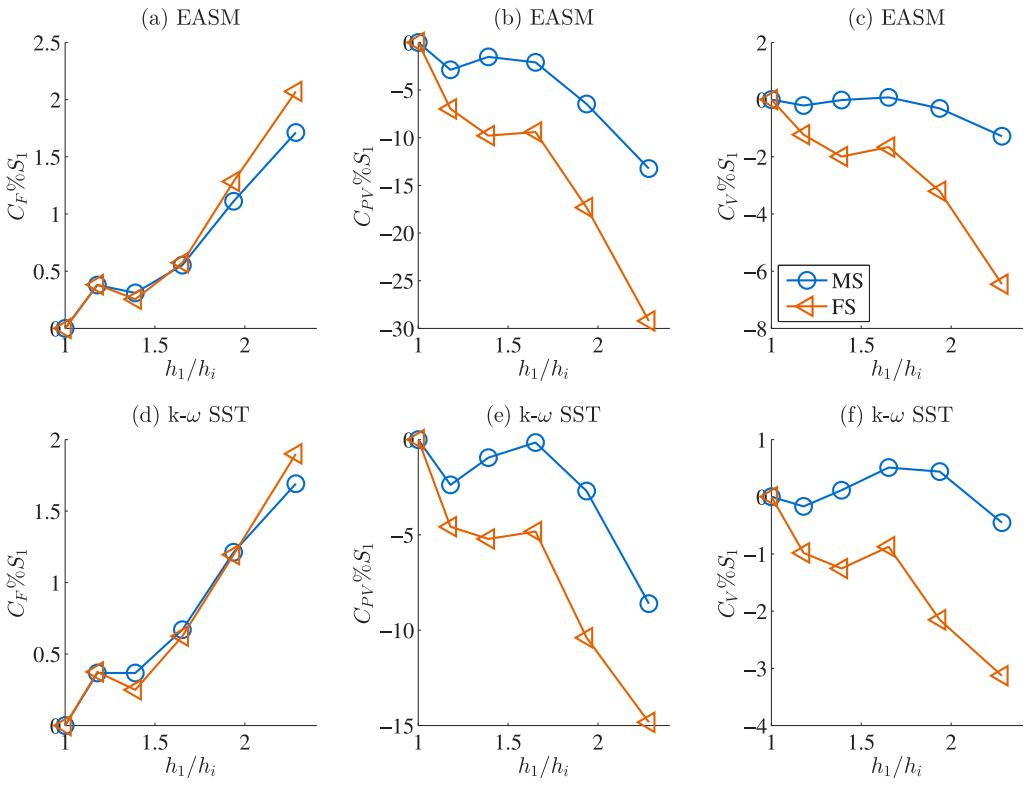

Fig. 6. Computed values for H1 test case: (a) C_F, (b) C_{PV} and (c) C_V with the EASM model and (d) C_F, (e) C_{PV} and (f) C_V with the $k-\omega$ SST model vs. grid refinement ratio, h_1/h_i.

the viscous flow around the stern but also the wave pattern upstream and the relation between the hydrodynamic and the hydrostatic pressure at the transom edge (Larsson and Raven, 2010; Starke et al., 2007). Therefore, investigation of the flow behind the transom only with a double-body RANS approach can be misleading unless the transom flow is reasonably similar with and without a free-surface. Therefore, DB and FS RANS computations were performed to investigate the flow behind the transom with and without a free-surface, in model and full-scale.

The scale effects on the stern wave system and the wetted-transom flow between the model and full-scale require further consideration for the full-scale FS RANS computations. The primary source of this scale effect is the different boundary layers around the stern between the model and full-scale, as suggested by Raven et al. (2008) and Farkas et al. (2017, 2018). As a newly built ship at the sea trial cannot be hydrodynamically smooth but with a certain hull roughness, its effect on the boundary layer should also be assessed. Otherwise, an FS RANS computation with hydrodynamically smooth surfaces will predict a thinner boundary layer in full scale than the actual ship. As a result, the pressure distribution around the stern and the wave pattern aft of the transom will differ. The hull roughness can especially be critical when the wetted-transom flow is in a transitionary phase. Therefore, the full-scale FS RANS computations included the hull roughness effect, which affects the boundary layer, the pressure distribution, and the wave pattern around the stern. The roughness is implemented by a modification of the boundary conditions for the specific dissipation rate (ω) and the turbulent kinetic energy (k) as explained by Orych et al. (2021). The roughness value used for the computations is quantified by the sand grain roughness equivalent to the standard hull roughness value recommended by ITTC (2021a). Since the main goal is to use the full-scale form factors in the extrapolation process, double-body computations were performed with no roughness effects as required by the form factor hypothesis (Hughes, 1954). Both DB and FS computations were performed at fixed even keel conditions, i.e. dynamic sinkage and trim were omitted to compare the same transom submergence levels for each loading condition.

In Fig. 7, the flow behind the transom in full scale is presented for the FS (Figs. 7(a), 7(c), and 7(e)) and DB (Figs. 7(b), 7(d), and 7(f)) RANS computations. All computations were post-processed at the same camera angle, and hulls are situated at the same location in the figures. The streamlines were generated from seeding 20 equidistant points behind the transom for both computation types. The colour of the streamlines was determined by the non-dimensionalised speed, u/U, where u is the local velocity, and U is the free stream velocity. The light blue isosurface in Fig. 7, represents $u/U = 0$ condition, hence, signifying the separated flow. Additionally, the free-surface is visualised by a transparent light purple isosurface for the FS RANS computations.

In order to be able to use double-body computations for the form factor calculations, it should be ensured that the flow behind the transom is reasonably similar for both FS and DB approaches when the transom is substantially submerged. Starting from the original scantling draught in full scale (Figs. 7(e) and 7(f)), it can be observed that the recirculating flow region (light blue surface) extends approximately to the same longitudinal position. A large dead-water region does not trail the side of the transom in both FS and DB approaches. The flow pattern is also notably similar, as indicated by the streamlines and the grey-coloured arrows visualising the flow directions. The slightly larger size of the recirculation region in free-surface computation is caused mainly by the interference of the large bow wave crest and the stern waves.

The next loading condition is T=$T_{scantling} - 1m$ which has the submerged transom area equals to 10% of the maximum cross-section area ($tr_{ratio} = 0.10$). The observations on the flow features seen in Figs. 7(c) and 7(d) is similar to the original $T_{scantling}$ draught. The free-surface does not seem to play a major role, and the double-body assumption seems to capture the major flow characteristics behind the transoms of the two deepest draughts. When the transom submergence is reduced one step further ($T = T_{scantling} - 2m$), some differences appear in the shape of the recirculation zone, namely the side of the transom. In double-body computations, the dead-water zone abruptly vanishes, moving from the centre line to the side of the transom. However, FS

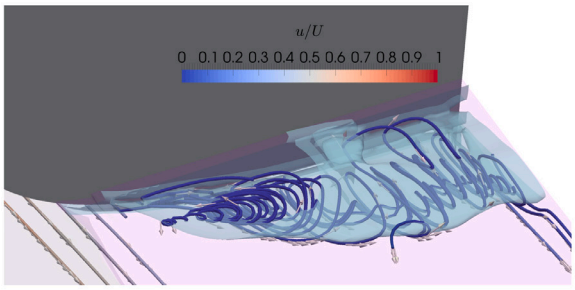

(a) FS RANS at $T=T_{scantling} - 2m$, $Fr_t = 2.29$, $tr_{ratio} = 0.043$

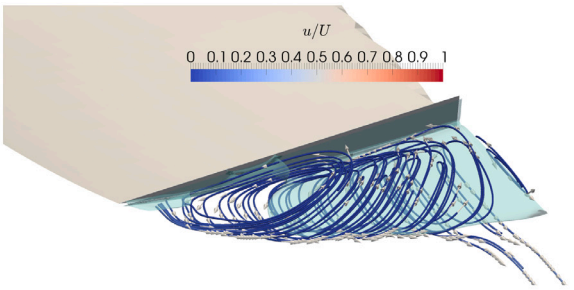

(b) DB RANS at $T=T_{scantling} - 2m$, $Fr_t = 2.29$, $tr_{ratio} = 0.043$

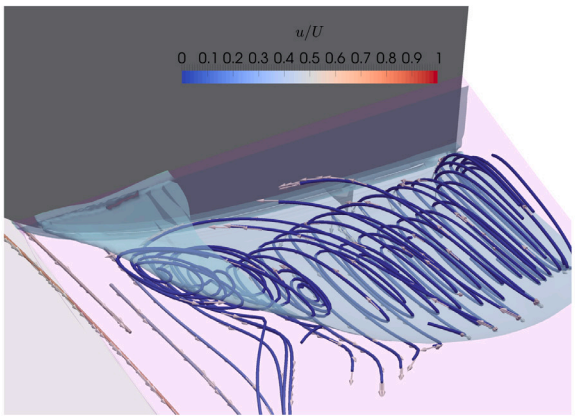

(c) FS RANS at $T=T_{scantling} - 1m$, $Fr_t = 1.62$, $tr_{ratio} = 0.10$

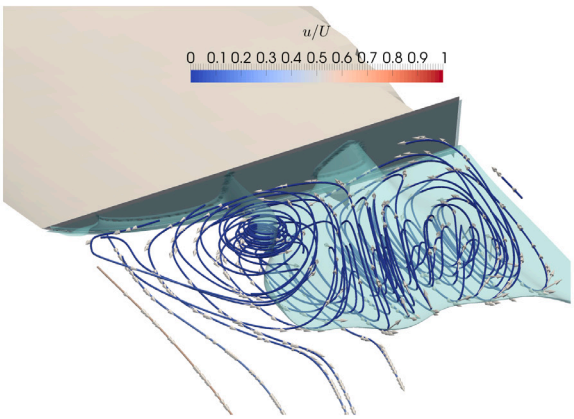

(d) DB RANS at $T=T_{scantling} - 1m$, $Fr_t = 1.62$, $tr_{ratio} = 0.10$

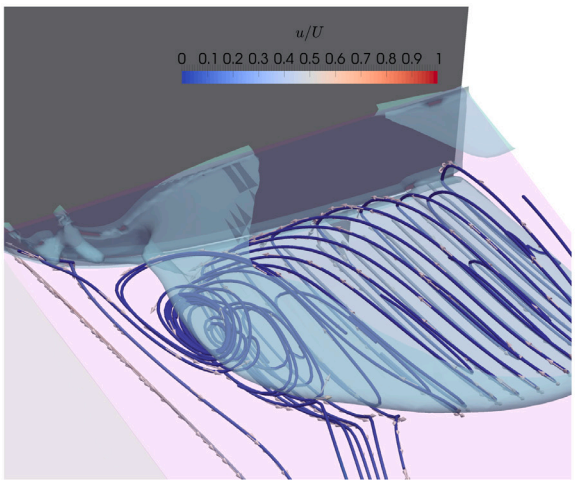

(e) FS RANS at $T=T_{scantling}$, $Fr_t = 1.37$, $tr_{ratio} = 0.16$

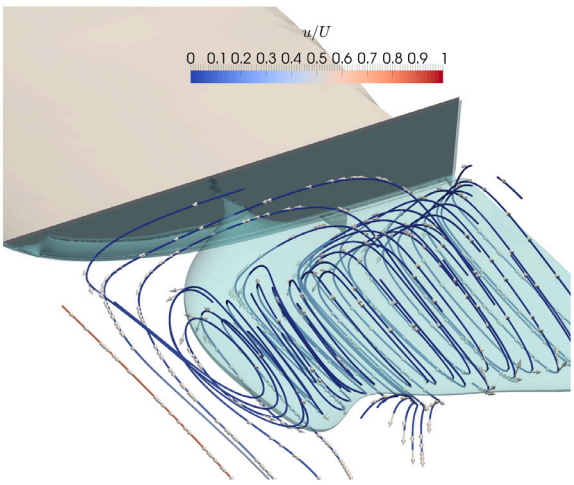

(f) DB RANS at $T=T_{scantling}$, $Fr_t = 1.37$, $tr_{ratio} = 0.16$

Fig. 7. Local flow behind the transom of the H1 test case (port side only) at various draughts at *full scale* at $Fr = 0.172$ using EASM turbulence model. (For interpretation of the references to colour in this figure legend, the reader is referred to the web version of this article.)

RANS results indicate a more gradual shrinkage of recirculating flow region, as observed in Fig. 7(a). This difference between DB and FS computations may lead to slightly under-predicted form factors for the cases where the transom submergence is rather small as the momentum loss can be slightly more in DB than the FS computation.

The comparison of DB and FS RANS computations in model scale are presented in Fig. 8. The conclusions from the comparison of full-scale results are also mostly valid in model scale. The flow characteristics from DB and FS are mainly similar at the original scantling draught and $T_{scantling} - 1m$. However, the light loading condition, $T_{scantling} - 2m$, shows a more significant difference in model scale than the full-scale when DB and FS results are compared. The recirculation region is notably smaller in double-body compared to free-surface, extending to the transom's side. This observation is somewhat expected since the role of the boundary layer, and the hydrodynamic pressure distribution at the transom becomes ever more critical when the submergence is decreased. Further decrease of transom submergence will lead the turbulent shear layer to create free-surface fluctuations, then give way to spill breakers, and eventually ventilation of the transom. As indicated by Maki (1997), the transition from wetted-transom to dry-transom flow regime (and vice versa) is strongly unsteady. Moreover, partially wetted-transoms are subjected to significant scale effects (Starke et al.,

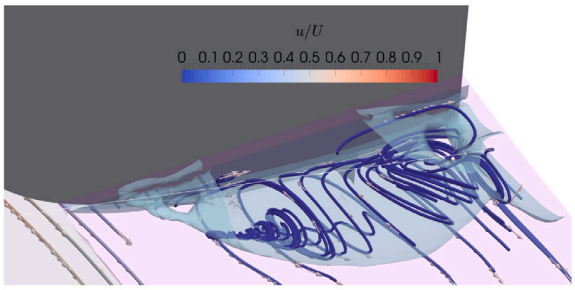

(a) FS RANS at $T=T_{scantling} - 2m$, $Fr_t = 2.29$, $tr_{ratio} = 0.043$

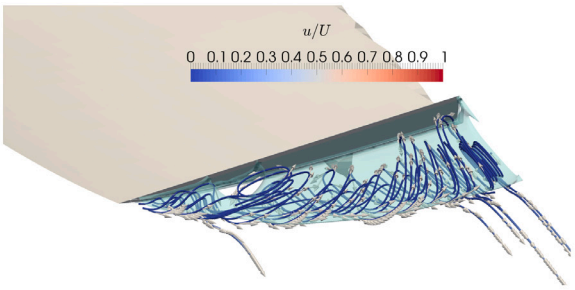

(b) DB RANS at $T=T_{scantling} - 2m$, $Fr_t = 2.29$, $tr_{ratio} = 0.043$

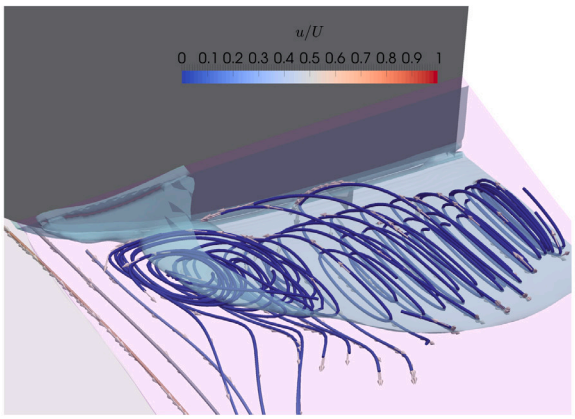

(c) FS RANS at $T=T_{scantling} - 1m$, $Fr_t = 1.62$, $tr_{ratio} = 0.10$

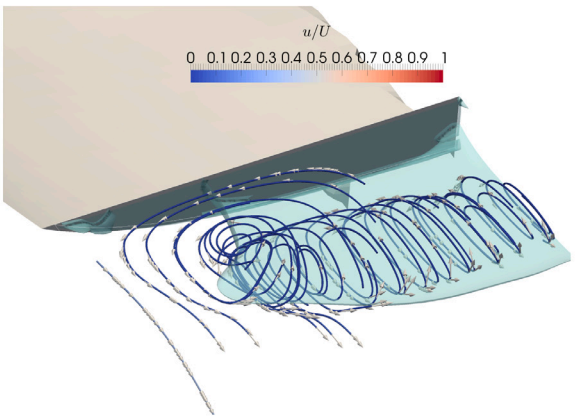

(d) DB RANS at $T=T_{scantling} - 1m$, $Fr_t = 1.62$, $tr_{ratio} = 0.10$

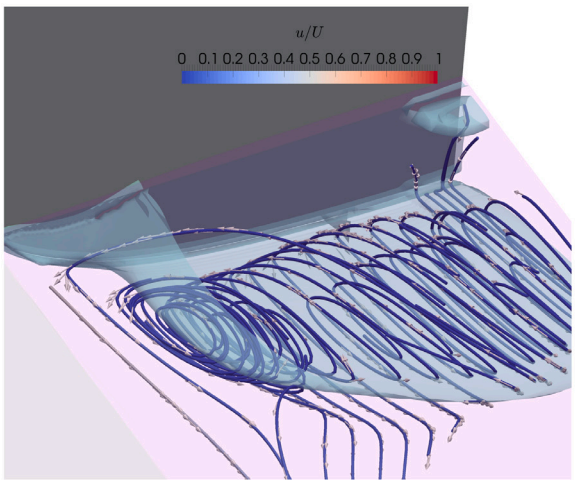

(e) FS RANS at $T=T_{scantling}$, $Fr_t = 1.37$, $tr_{ratio} = 0.16$

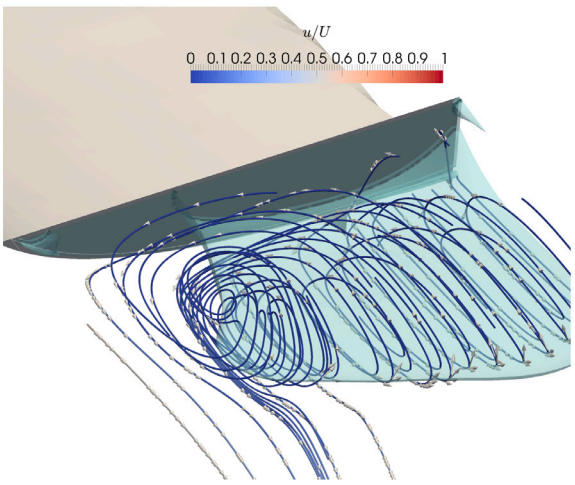

(f) DB RANS at $T=T_{scantling}$, $Fr_t = 1.37$, $tr_{ratio} = 0.16$

Fig. 8. Local flow behind the transom of the H1 test case at various draughts at *model scale* at $Fr = 0.172$ using EASM turbulence model.

2007). Therefore, the partially wetted transoms are outside this study's scope as the double-body computations cannot simultaneously capture the correct flow physics in model and full-scale.

6.2.2. Characterisation of the flow and the scale effects

As shown earlier, the flow behind the transom is largely similar for double-body and free-surface computations when the transom is substantially submerged. Therefore, the local flow of H1 is suitable for further investigation using the DB computations. In Fig. 9, the u/U contours have been presented for model and full-scale at a position that is slightly behind the transom ($x/L_{PP} = -0.03$ where $x/L_{PP} = 0$ is the aft perpendicular). As expected, velocity contours indicate that u/U is shrinking in the region outside the wake of the transom from model to full-scale. However, the flow behind the transom shows little to no change even though the Reynolds number is greatly increased from model to full-scale. The limiting streamlines are generated at the $x/L_{PP} = -0.03$ and $x/L_{PP} = -0.13$ slices together with the u/U contours as presented in Fig. 10. The limiting streamlines just behind the transom indicate only marginal difference between model and full-scale as can be seen from the Figs. 10(a) and 10(c). Except at both ends of the transom edge (bold black line), the limiting streamlines converge behind the transom (similar to a vortex sheet separation). They follow nearly identical paths in model and full-scale. When the flow downstream is investigated as shown in Figs. 10(c) and 10(d), a large vortex is observed near the side of the transom for both model and full-scale. In addition, the bilge vortex can also be seen at approximately $z/l_{PP} = 0.04$ near the centre plane. When model and full-scale computations are compared, the wake behind the hull, including the bilge vortex size, shrinks with the increasing Re. However, the same cannot be stated for the large vortex generated behind the transom. These observations are

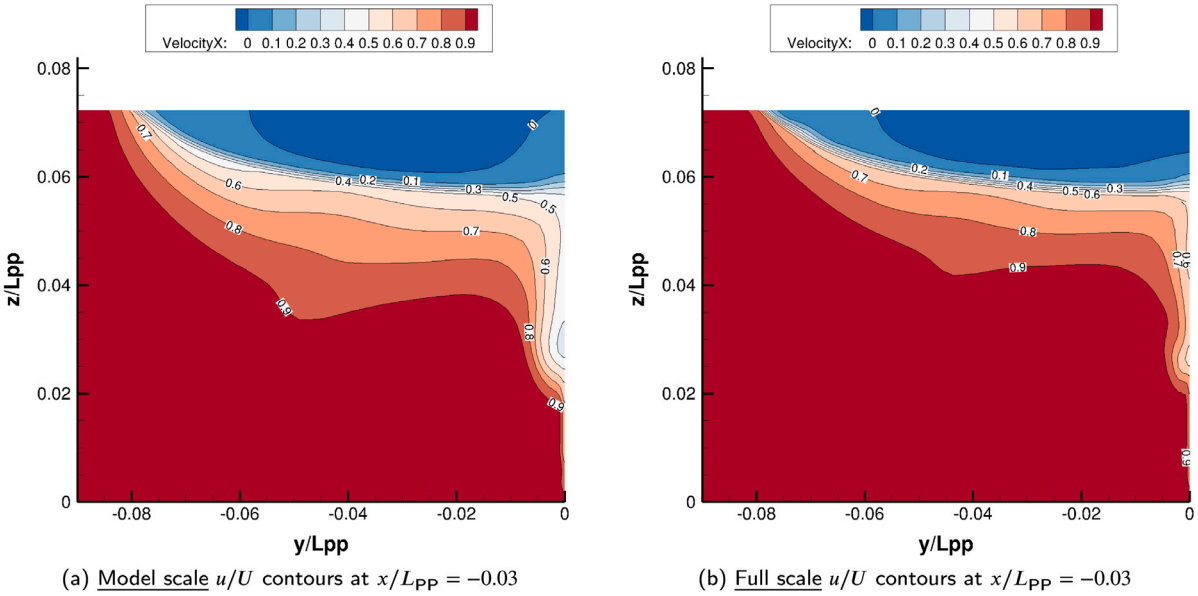

Fig. 9. Local flow behind the transom of the H1 test case at scantling draught at model (left) and full (right) scale using EASM turbulence model.

the foundation reasons for the authors to propose dividing the C_{PVM} term, i.e. form resistance (Hughes, 1954), into two parts (Eq. (4)): C'_{PVM} and C_{trM}. The former term aims to capture the change of C_{PVM} proportional to the frictional resistance coefficient, while the latter term represents the part of the form resistance that is not proportional to C_F.

The u/U contours with limiting streamlines are presented in Fig. 11 for the other two draughts, $T_{scantling} - 2m$ and $T_{scantling} - 1m$. The local flow for the latter loading condition shows the same tendencies as the deepest draught. However, the lightest draught indicates a somewhat different local flow between model and full-scale. The clearly defined converged limiting streamlines disappeared as opposed to the other conditions. Instead the limiting streamlines are converged to approximately $y/l_{PP} = 0.03$ at model scale and $y/l_{PP} = 0.02$ in full scale.

6.2.3. The effect of turbulence modelling

The prediction of the local flow quantities in the stern region is highly dependent on the choice of the turbulence model, as concluded at the 2015 Tokyo CFD Workshop (NMRI, 2015). The comparison of the extensive local flow measurements and the CFD results with varying turbulence models indicated that two-equation models underpredict the longitudinal vorticity significantly compared to the anisotropic models (Hino et al., 2020). On the other hand, the mean absolute error of resistance predictions in the Tokyo 2015 Workshop (as well as in the 2010 Gothenburg Workshop Larsson et al., 2014) was smaller for the two-equation models than for the anisotropic models. Therefore, it is relevant to investigate further the local flow obtained from k-ω SST and EASM turbulence models. In Fig. 12, the iso contours of the second invariant of the velocity gradient tensor $Q = 10$ (coloured by vorticity) are presented together with the streamlines around the transom using the same grid (double-body assumption) with k-ω SST and EASM turbulence models in model scale. It can be observed in Fig. 12(a) that even with definitive V-type stern sections, a bilge vortex is generated, and its extension is marked by the Q iso surface from the results from EASM. However, k-ω SST indicates a relatively weak longitudinal vorticity as the Q iso-surface following the stern bulb dies out quickly. Similar observations were also concluded by Hino et al. (2020) since more longitudinal vorticity with the EASM turbulence model was associated with increased vorticity production thanks to turbulence anisotropy.

The large vortex initiated from the side of the transom, which was also highlighted in Fig. 10(c), are clearly depicted by the iso contours of the second invariant of the velocity gradient tensor for both turbulence models as seen in Fig. 12. It is worth mentioning that the difference between the turbulence closures is significantly less for the vortex trailing the side of the transom compared to the vortex trailing the stern bulb. This observation can be explained by the role of the boundary layer in making the vortices. As argued earlier, the flow behind the substantially submerged transoms is not too dependent on the boundary layer generated along the hull. The recirculating flow region, however, shows modest differences between the two turbulence models. The iso wake contours (u/U) from the k-ω SST and the EASM turbulence models are presented in Fig. 13 which shows that the flow reattachment point is further downstream for the EASM compared to the k-ω SST both in model and full-scale. In other terms, the recirculation region is slightly larger for the EASM turbulence model as it is commonly observed for the non-linear anisotropic turbulence closures (Hino et al., 2020). It is concluded that there are indeed minor differences in resistance and the local flow predictions between the two turbulence models. However, the main conclusions about the flow characteristics and scale effects are valid for both turbulence closures.

6.3. Quantitative analysis of results

In this section, the results of approximately 450 double-body computations will be investigated quantitatively. This analysis is initially aimed to check if there are relationships between the relative change of form factors from model to full-scale and the geometrical transom parameters (see Section 3), ship hydrostatics, and the Reynolds number. In case definitive relations are discovered, the next goal of the quantitative analysis is to describe these relations with an equation, as explained in the next section, so the corrections for the transom submergence can be applied even without using CFD.

All seven hull forms were computed at their respective design or scantling draughts and additional draughts with even keel conditions in model and full-scale. Except for the KCS hull form, the other hulls already featured submerged transom at their respective design or scantling draughts. Therefore, the selection of additional draughts other than the original loading conditions was made to cover lighter and heavier loading conditions. However, the KCS hull form was only submerged more than the original design draught in successive steps. Additionally, the effect of trim was investigated on two hull forms by trimming the vessels by the bow and stern. The pivot point for applying the trim was the midship of the vessels, and summation of the change in forward

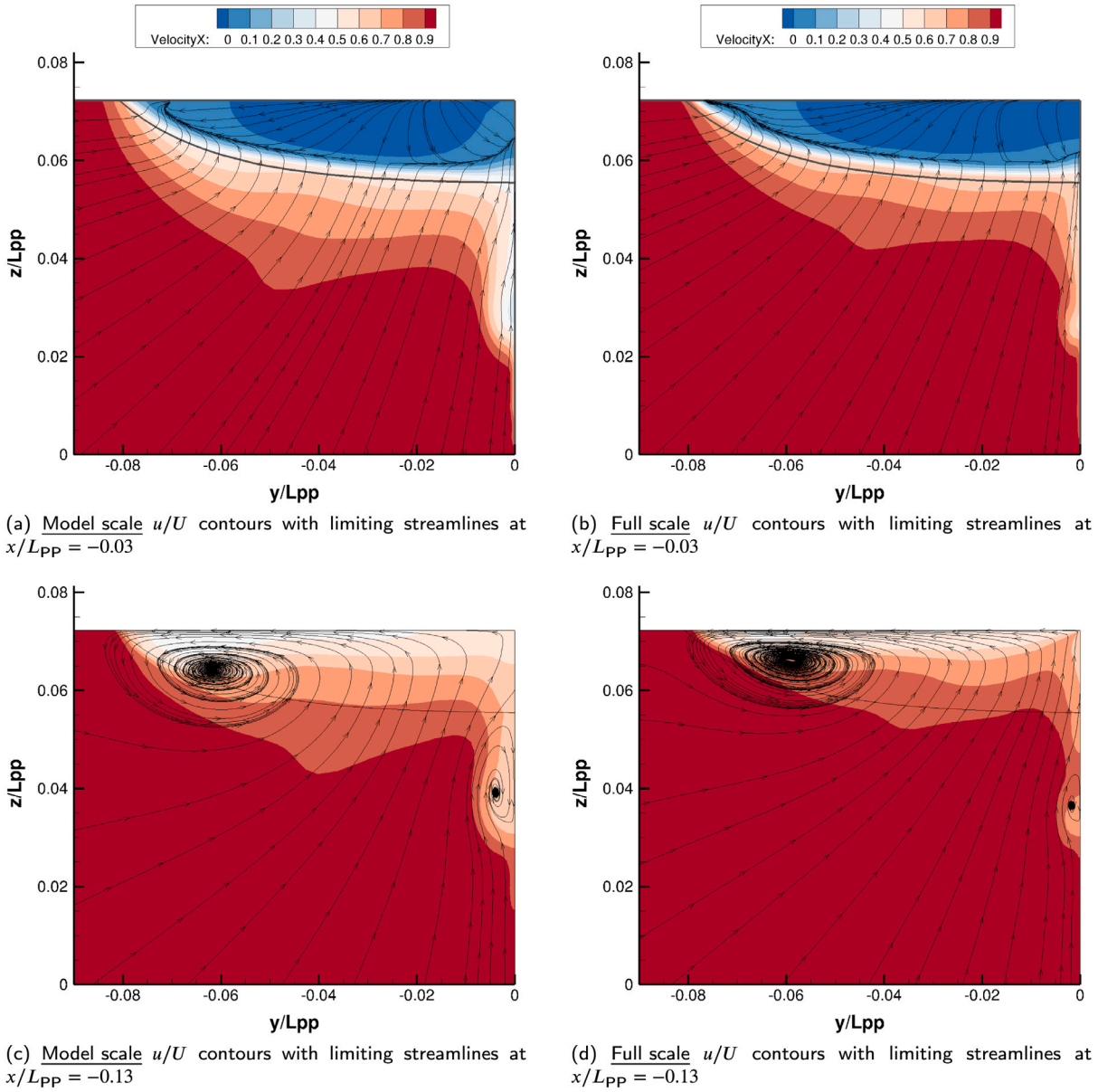

(a) Model scale u/U contours with limiting streamlines at $x/L_{PP} = -0.03$

(b) Full scale u/U contours with limiting streamlines at $x/L_{PP} = -0.03$

(c) Model scale u/U contours with limiting streamlines at $x/L_{PP} = -0.13$

(d) Full scale u/U contours with limiting streamlines at $x/L_{PP} = -0.13$

Fig. 10. Local flow behind the transom of the H1 test case at scantling draught ($T_{scantling}$) at model (left column) and full (right column) scale using EASM turbulence model.

and aft draughts equated to the trim. Finally, the same two hulls were also used for investigating the Reynolds Number effects by varying the "scale factor" of the model.

The qualitative analysis of the flow behind the substantially submerged transom revealed that the flow separation is neither disappearing nor shrinking proportionally to the frictional resistance coefficient. Therefore, using the standard ITTC-78 method for the resistance extrapolation (i.e. the Hughes (1954) form factor assumption) will result in under-prediction of the viscous resistance, as illustrated in Fig. 2. On the other hand, in the case of a hull with a bubble type separation in model scale and without a transom stern submergence, the effect is the opposite since this flow separation is likely to diminish in full scale; hence, the viscous resistance will be over-predicted. In order to quantify the deficiency (transom submergence) or the surplus (bubble type separation) of the extrapolated full-scale viscous resistance, the "error" caused by the Hughes hypothesis when there is flow separation can be expressed as

$$E = C_{VS} - C'_{VS} \,, \tag{9}$$

where C_{VS} is the true full-scale viscous resistance, and C'_{VS} is the extrapolated full-scale viscous resistance based on the standard ITTC-78 method (see Fig. 2). In this study, C_{VS} is directly obtained from the full-scale double-body RANS computations, while C'_{VS} is calculated as

$$C'_{VS} = C_{FS}(1 + k_M) \,, \tag{10}$$

where C_{FS} is the full-scale frictional resistance coefficient obtained from a friction line, and k_M is the CFD based form factor obtained from model-scale DB RANS computations.

The error defined in Eq. (9) can represent the two different separation types;

- persistent separation, which occurs in both model and full-scale (e.g. large transom submergence),

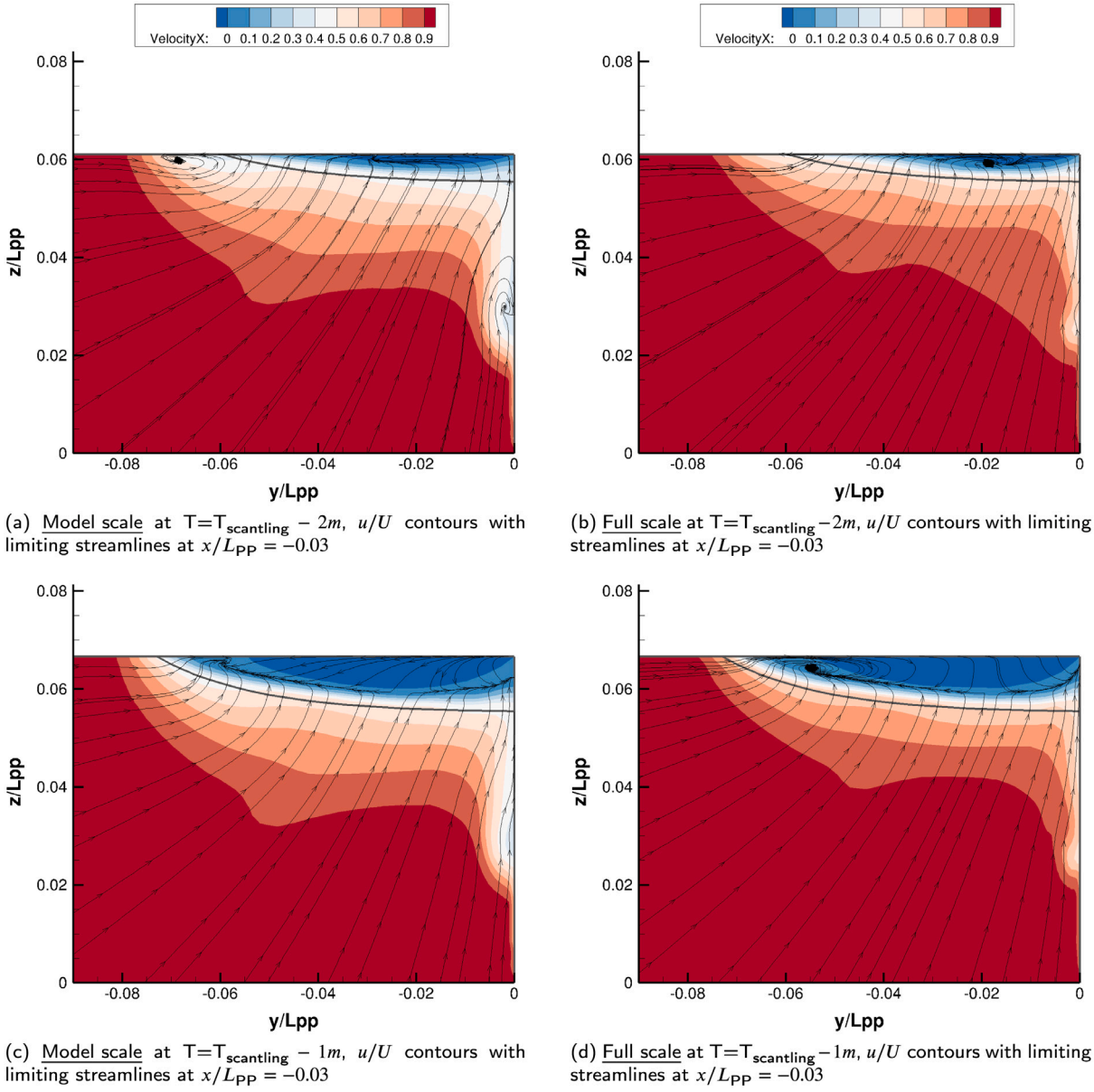

(a) Model scale at T=$T_{scantling} - 2m$, u/U contours with limiting streamlines at $x/L_{PP} = -0.03$

(b) Full scale at T=$T_{scantling} - 2m$, u/U contours with limiting streamlines at $x/L_{PP} = -0.03$

(c) Model scale at T=$T_{scantling} - 1m$, u/U contours with limiting streamlines at $x/L_{PP} = -0.03$

(d) Full scale at T=$T_{scantling} - 1m$, u/U contours with limiting streamlines at $x/L_{PP} = -0.03$

Fig. 11. Local flow behind the transom of the H1 test case at various draughts at model (left column) and full (right column) scale using EASM turbulence model.

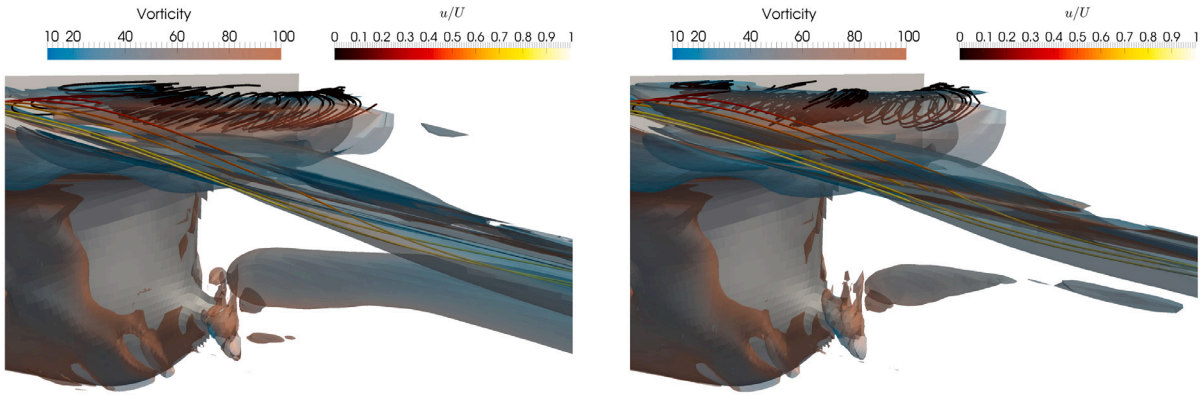

(a) EASM

(b) k-ω SST

Fig. 12. The iso contours of the second invariant of the velocity gradient tensor, $Q = 10$, at the stern of H1 at scantling draught and model scale. (For interpretation of the references to colour in this figure legend, the reader is referred to the web version of this article.)

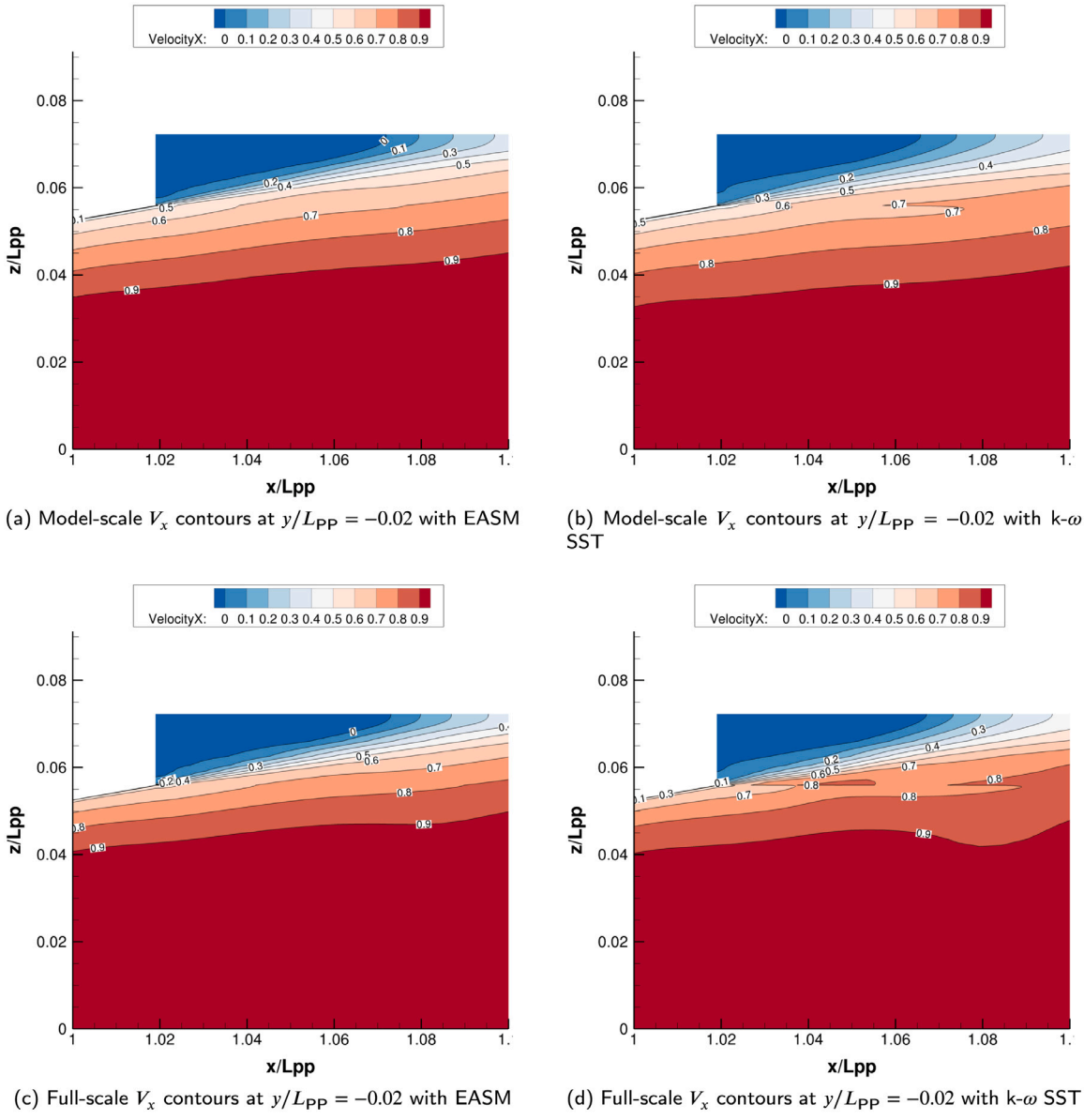

(a) Model-scale V_x contours at $y/L_{PP} = -0.02$ with EASM

(b) Model-scale V_x contours at $y/L_{PP} = -0.02$ with k-ω SST

(c) Full-scale V_x contours at $y/L_{PP} = -0.02$ with EASM

(d) Full-scale V_x contours at $y/L_{PP} = -0.02$ with k-ω SST

Fig. 13. Local flow behind the transom of the H1 test case at scantling draught at model (left column) and full (right column) scale.

- and separation occurs in model scale but not in full scale (e.g. bubble type separation around the stern bulb).

The error term in Eq. (9) can also be expressed similar to a form factor,

$$k_{error} = \frac{C_{VS} - C'_{VS}}{C_{FS}} = \frac{C_{FS}(1 + k_S) - C_{FS}(1 + k_M)}{C_{FS}} \tag{11}$$

where $C_{FS}(1 + k_S)$ is the viscous resistance obtained from the full-scale CFD computation, $C_{FS}(1 + k_M)$ is the extrapolated full-scale viscous resistance using the model-scale form factor, and C_{FS} is the full-scale frictional resistance coefficient obtained from a friction line. Formulation of the error similar to a form factor makes the quantification of the error possible to perform one computation at each scale instead of computations carried out at each speed. The Eq. (11) will not be valid; however, if the flow separation size and character vary significantly within the model-scale Reynolds numbers. For example, a vessel with a substantially submerged transom for which the transom does **not** run wet throughout the speed range is not too suitable for the form factor representation of the error as in Eq. (11).

As discussed in Section 2, the viscous pressure resistance was decomposed into C'_{PVM} and C_{trM} where the latter indicated the form resistance that is not proportional to the friction line. Keeping Fig. 2 in mind and assuming that there is no bubble-type flow separation at the stern (which is true for all test cases used in this study), the formulation of k_{error} can also be written as

$$k_{error} \simeq k_{tr} = \frac{C_{trS}}{C_{FS}} \ . \tag{12}$$

where k_{tr} is called as the *transom form factor*. Hence, the deficit of the viscous resistance when the model-scale form factor, k_m, was used for the extrapolation from model to full-scale is quantified as k_{tr} shown in Eq. (12). As discussed in Section 6.2, the flow separation is persistent for the case of a substantial transom in both model and full-scale hence C_{trS} must exist. However, when there is no submerged transom and no flow separation in the flow, C_{trM} and C_{trS} terms disappear (as in Fig. 1) and the form factor in model and full-scale becomes equal. This hypothesis (Hughes, 1954) was thoroughly tested by Korkmaz et al. (2020, 2021, 2019a), and confirmed that the form factors in model and full-scale are nearly the same when there is no flow separation in the flow, and an appropriate friction line is used. In order to disregard the

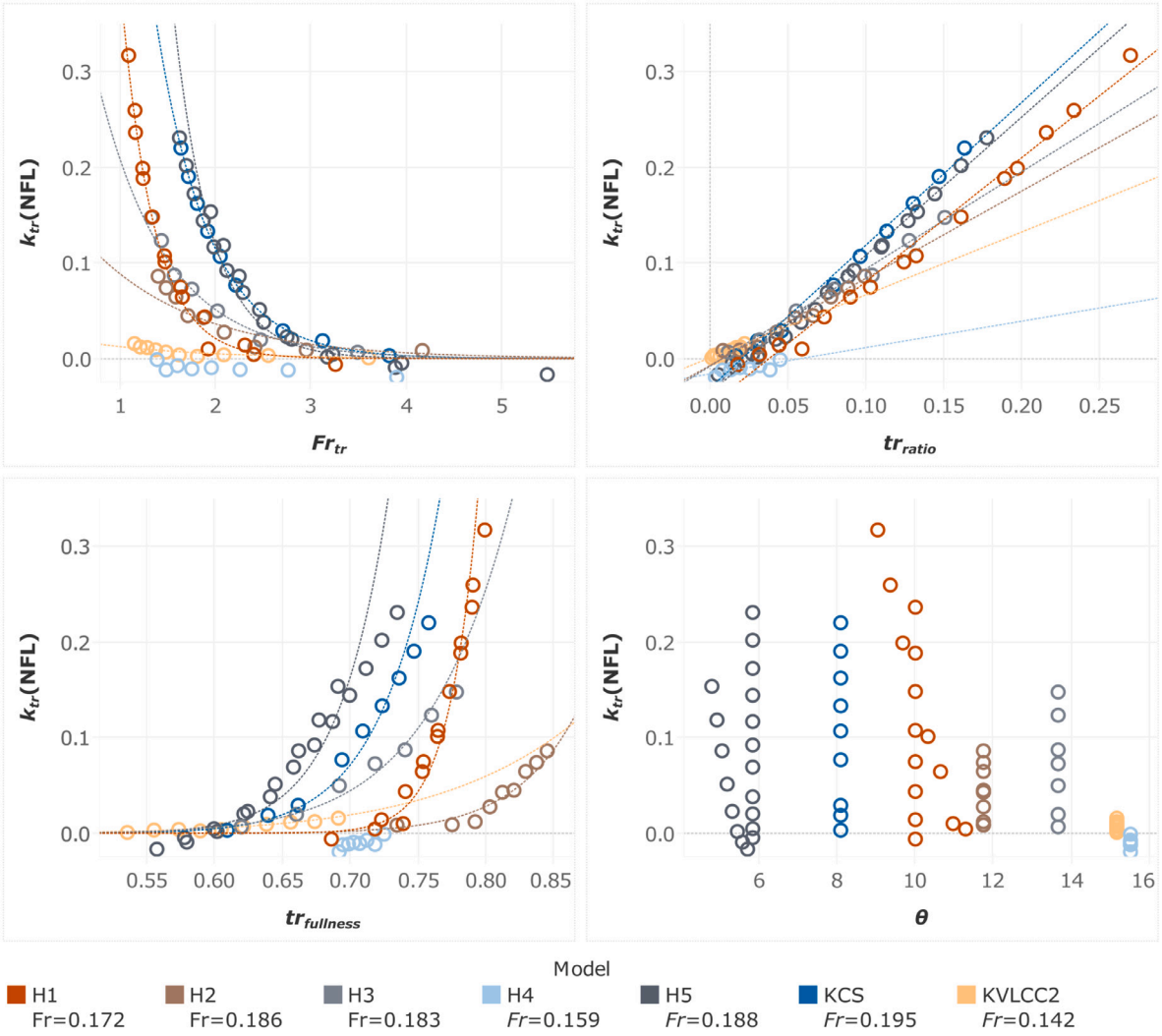

Fig. 14. Transom form factors with k-ω SST model vs. transom parameters; transom Froude number (top left), tr_{ratio} (top right), $tr_{fullness}$ (bottom left), and θ (bottom right). (For interpretation of the references to colour in this figure legend, the reader is referred to the web version of this article.)

scale effects on form factor caused by the usage of the ITTC-57 model to ship correlation line, the two numerical friction lines (NFL) (Korkmaz et al., 2019b) of the same CFD code and turbulence model were used. It was shown in Korkmaz et al. (2021) that usage of NFLs nearly eliminated the speed dependency of CFD based form factors. Therefore, quantification of C_{trS} term will be more accurate when the NFLs are used rather than the ITTC-57 line.

The transom form factor values have been calculated using the numerical friction line (Korkmaz et al., 2019b) and plotted in Fig. 14 against the transom parameters explained in Section 3. The Froude number of each test case is constant and noted in the legend of Fig. 14. The first parameter to investigate is Fr_{tr}, which is often used as an indicator (even with limited validity) of the flow regime behind the transom. As observed in the top-left Fig. 14, the k_{tr} values of all hulls (except H4) reasonably follows the exponential curves fitted for each hull. An exponential curve cannot be fitted to the k_{tr} values of H4 since they are slightly below zero, which indicates that flow separation behind the transom disappeared or decreased its size when the Re is increased from model to full-scale. The second observation is that there are three distinct clusters of points as the Fr_{tr} decreases, which is equivalent to increased transom submergence as the speed was kept the same. The three different clusters are in line with the type of vessels; the flattest curve is followed by the very large, high block, slow steaming vessels (H4 and KVLCC2); the cluster in the middle is medium to small sized high block vessels (H1, H2 and H3); the cluster of the point that follows the steepest curve are the slender and fast going vessels (H5 and KCS). As it is for determining the flow regime behind the transom, the Fr_{tr} values alone cannot indicate which k_{tr} values should be expected. However, all k_{tr} values tend to converge towards zero after $3.5 < Fr_{tr}$ where the flow regime is likely to be partially wetted or fully dry and not suitable for double-body computations.

The second transom parameter to investigate in Fig. 14 is tr_{ratio} (see Section 3). The ratio between the submerged area of the transom and the maximum cross-section area at rest indicates a highly linear correlation with the k_{tr} values. The linear lines fitted to the k_{tr} values of each hull indicate similar slopes for most hulls except the H4 and KVLCC2. It should also be noted that as the tr_{ratio} values decreases, k_{tr} values converge towards zero ($k_M \approx k_S$) as expected.

The third parameter, $tr_{fullness}$, indicates how full the transom edge section is, and it is presented in the bottom right scatter plot in Fig. 14. It can be observed that no specific trend exists neither among the hulls nor similar ship types. Hence, the V-shaped or U-shaped transom seems to play little to no role in the quantity of the transom form factor.

The last parameter plotted in Fig. 14 against the k_{tr} is the slope of the stem profile near the transom, θ (see Fig. 3(b)). Similar to $tr_{fullness}$, the θ angle does not appear to have a significant effect on k_{tr}. Instead, the submerged transom area can be regarded as the most influential parameter for the transom form factor. In other terms, the size of the

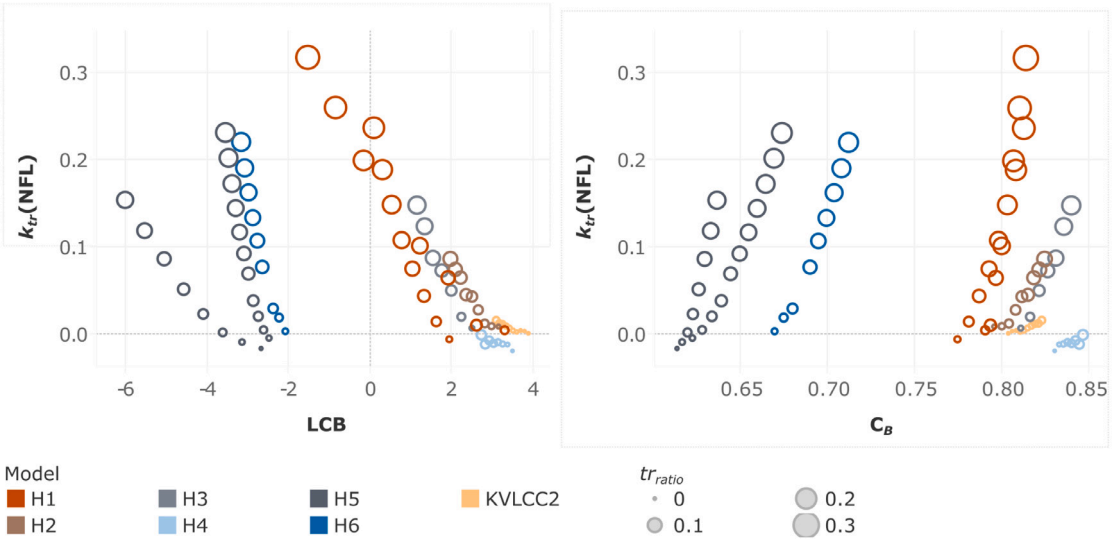

Fig. 15. Transom form factors with k-ω SST model versus hydrostatics; centre of buoyancy, rel. to $L_{PP}/2$ (left), block coefficient (right).

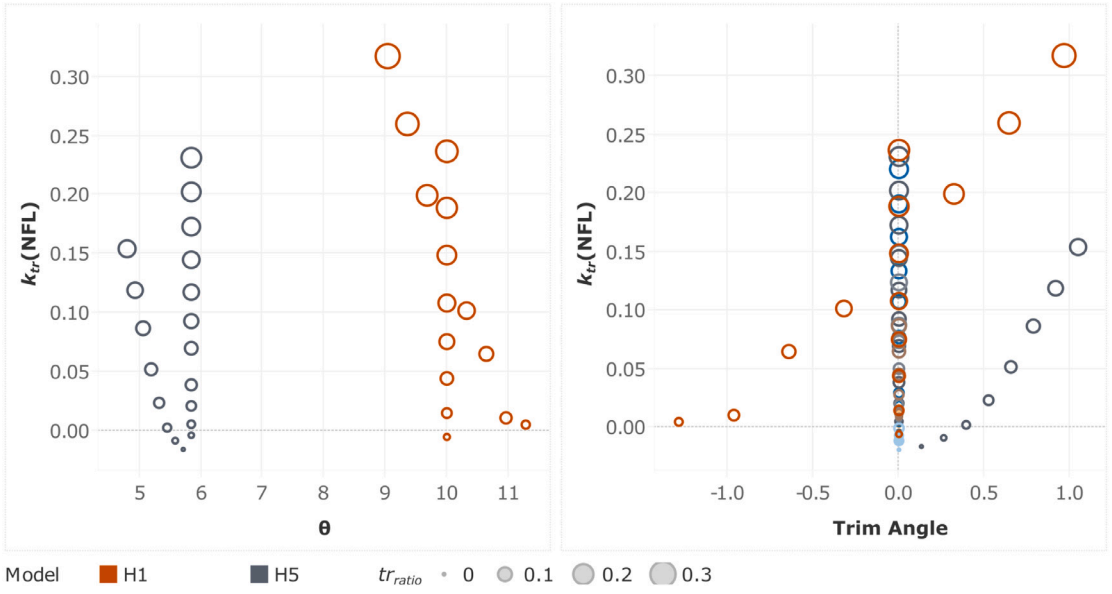

Fig. 16. Transom form factors with k-ω SST model versus trim angle (right) and stem profile angle near transom (left).

viscous resistance deficiency, C_{trS}, is mainly dependent on the area of the submerged transom.

In addition to the transom parameters, hydrostatics are compared against k_{tr} values. As presented in Fig. 15; LCB, and C_B are plotted against the transom form factor. The same colour scheme is kept for distinguishing different hull forms, but the markers are sized with respect to tr_{ratio} values of the corresponding computation. It can be observed in Fig. 15 that changing the draught or trimming the vessel has a large effect on the hydrostatics. At first, increasing the block coefficient or shifting the LCB to stern may seem to increase k_{tr}. However, when the marker sizes (tr_{ratio}) are also taken into account, it can be argued that the effect of hydrostatics on k_{tr} values is rather limited. As discussed earlier in Section 6.2, the recirculating flow did not largely dependent on the boundary layer generated along the hull, which will certainly be affected by the significant changes in the hydrostatics. Later investigations on LCB showed that the longitudinal centre of buoyancy is indeed instrumental in the determination of the slope of the linear tr_{ratio} vs k_{tr} relations between the high and low block vessels as explained in Section 7.

The two vessels trimmed around the midship, H1 and H5, are plotted against k_{tr} and presented in Fig. 16. The slender H5 vessel was only trimmed by the stern as the transom will rise out of the still water level if trimmed by the bow. As can be seen in Fig. 16, trimming the vessel by the stern has a substantial effect on the tr_{ratio}, and as a result, increases the k_{tr} values sharply. However, when the trim angle is considered together with the θ angle, it can be argued that trimming the vessel has no substantial effect on its own as quite different trim angles (or θ) with similar tr_{ratio} values result in similar k_{tr} values.

After the submerged transom area, the second most important factor is the Reynolds number at the model and full-scale for the size of the transom form factor. As argued earlier, the form factor is not independent of the Reynolds number in the case of a wetted-transom; hence, the difference between the model and full-scale form factors will increase or decrease when the model-scale or full-scale Re substantially changes. The model-scale Re of H1 and H5 were changed successively while the full-scale Re and loading condition kept the same, and the k_{tr} values were plotted against the Reynolds number and C_F in Fig. 17. As expected, the gap between the model and full-scale form factors, k_{tr}, decreases as the Re in the model scale increases.

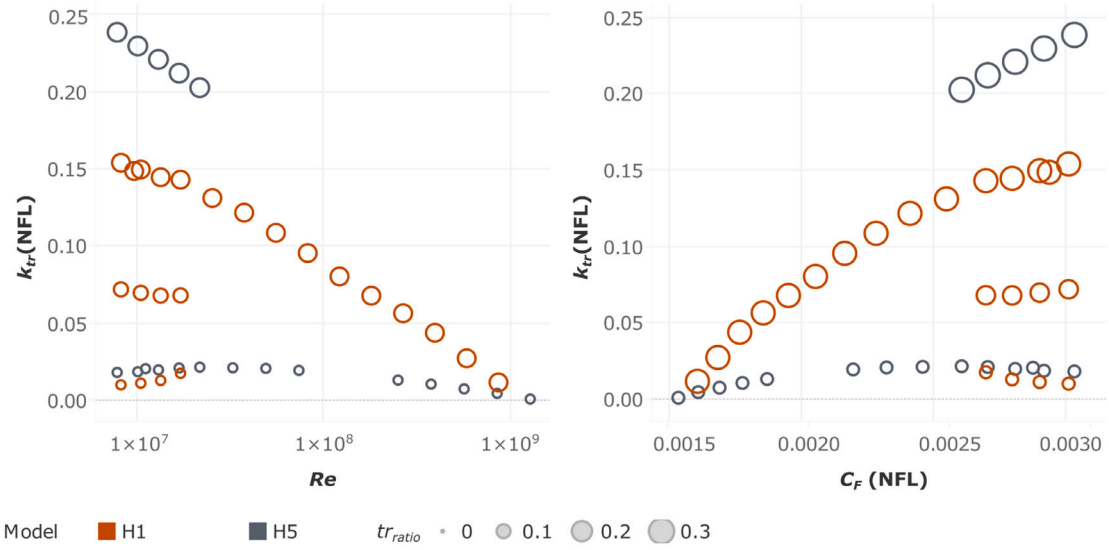

Fig. 17. Transom form factor with k-ω SST model against Reynolds number and frictional resistance coefficient derived from ITTC-57 line.

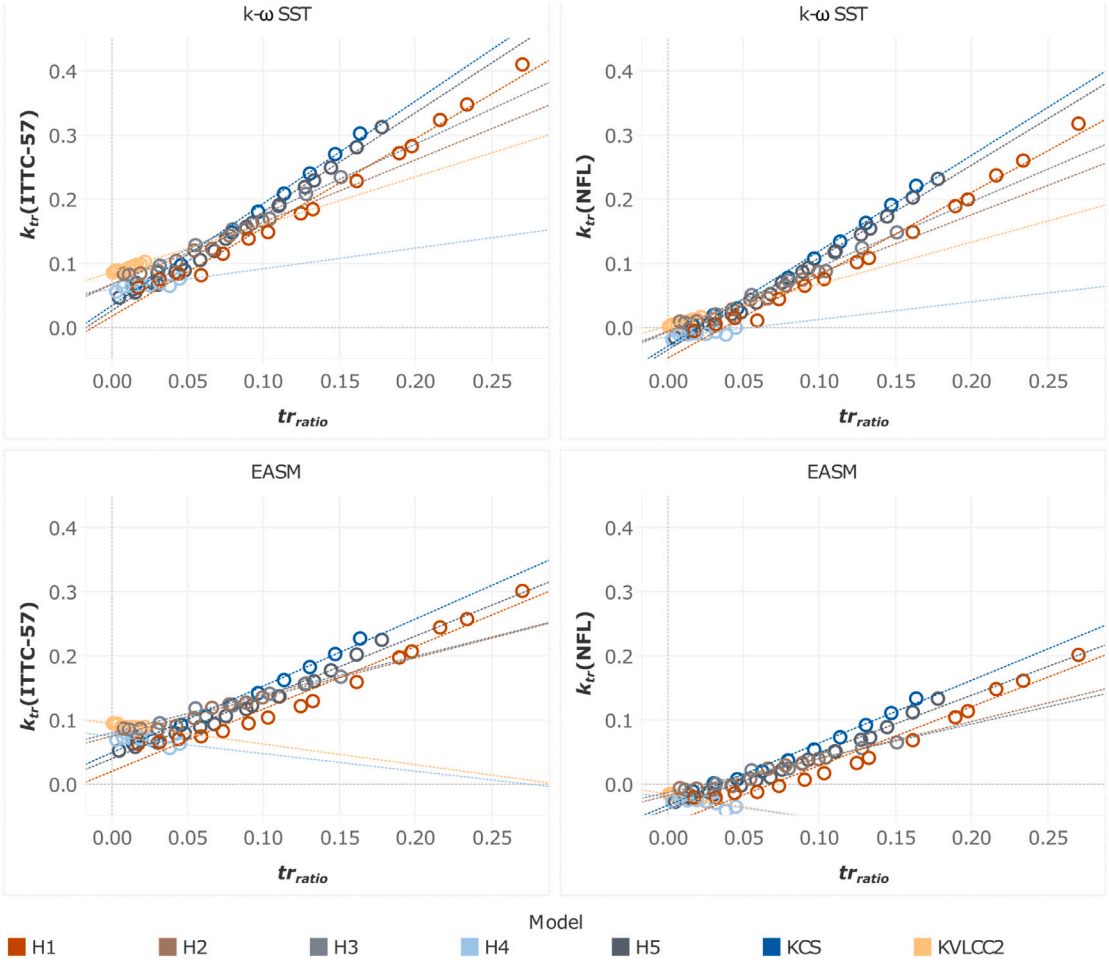

Fig. 18. Transom form factors based on ITTC-57 line (left column) and NFL (right column) for k-ω SST (top row) and EASM (bottom row) turbulence models.

The importance of the friction line for the CFD based form factors cannot be overstated since the validity of the form factor hypothesis (Hughes, 1954) entirely depend on it. Earlier studies (García Gómez, 2000; Toki, 2008; Pereira et al., 2017; Terziev et al., 2019; Wang et al., 2015; Korkmaz et al., 2020, 2021; Raven et al., 2008; Wang et al., 2015; Dogrul et al., 2020) indicated that there are scale effects on form factors when the ITTC-57 model to ship correlation line is used. However, scale effects on form factors were reduced with the usage of Katsui line (Katsui et al., 2005), and it nearly disappeared when numerical friction lines of the same code and turbulence model were used as the

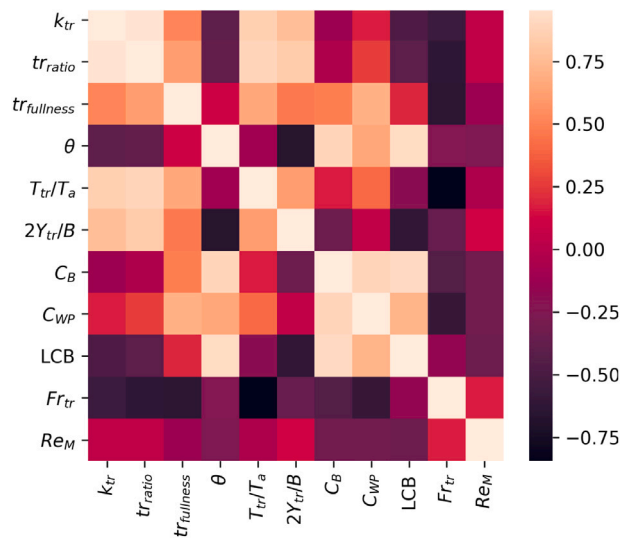

Fig. 19. Correlation matrix for the possible regression variables, colours represent the correlation values.

double-body RANS computation (Korkmaz et al., 2020). As can be seen in Fig. 18, the k_{tr} values when ITTC-57 line was used (indicated as k_{tr}(ITTC-57) in y-axis) approaches towards approximately 0.05 for both turbulence models when the tr_{ratio} is near zero, i.e. close to no transom submergence and no flow separation. Instead, the model and full-scale form factors should have been equal ($k_{tr} = 0$) as is observed when the numerical friction lines (indicated as k_{tr}(NFL) in the y-axis) were used, as shown in Fig. 18.

The other critical subject is the choice of turbulence closure which becomes more important when there is a flow separation. As can be seen in Fig. 18, the EASM model not only predicted lower k_{tr} values than the k-ω SST model in general but also presents a significantly lower slope of k_{tr} with regards to the tr_{ratio}.

7. An empirical correction for transom submergence

The existence of flow separation in model or full-scale makes the form factor approach of current recommended procedures for scaling of the towing tank tests (ITTC, 2021a) invalid, as noted by the ITTC (2021e, p. 11). As explained in Section 2, the $2-k$ method was proposed to take into account all kinds of flow separation, including the recirculating flow behind the transom. However, the $2-k$ *method* requires capabilities of double-body RANS computations in model and full-scale where an organisation is required to demonstrate (ITTC, 2021d): a Best Practice Guideline (BPG), quality assessment of the BPG, and demonstration of quality. An alternative empirical correction method is developed for

- a quick and approximate quantification of the transom form factor where many different loading conditions were model tested, such as trim optimisation tests,
- organisations that do not have the CFD capabilities.

The resistance caused by a wetted-transom can be explained in an analogy with airfoil shapes with truncated trailing ends. As explained in Starke et al. (2007), it can be considered that "the transom stern resistance as a 'base drag' as occurs on aerodynamic shapes with cutoff trailing ends. This base drag is caused by a reduction of the hydrodynamic pressure on the base, caused by the 'jet-pump' effect of the surrounding flow that exerts an entraining force on the recirculation region aft of the base". The investigations of Hoerner (1965) on projectiles and foil shapes with truncated trailing edges concluded that relatively simple equations could largely model the base drag. Therefore, an attempt has been made to obtain an empirical correction formula through a regression analysis of the results presented in Section 6.3.

The regression analysis is based on predicting the k_{tr} values from the k-ω SST model and the numerical friction line. As argued earlier and presented in Fig. 18, the k_{tr} values from the ITTC-57 line include the scale effects introduced by the friction line itself; hence, they cannot be used for quantification of viscous resistance deficit in full scale. Additionally, the form factor predictions from EFD and CFD in the model scale compared significantly better with the k-ω SST model.

The independent variables for the regression model are determined through an initial check on the correlation between the dependent variable, k_{tr}, and the correlation between the independent variables to sustain non-collinearity. The correlation matrix is presented in Fig. 19 for the dependent and all independent variables considered. It can be seen that the correlation between k_{tr} and tr_{ratio} is highest (0.98), while the correlation between k_{tr}, T_{tr}/T_a (where T_a represents draught at the aft perpendicular), and $2Y_{tr}/B$ variables are followed with 0.85 and 0.79. Keeping in mind Fig. 3, tr_{ratio} parameter can be considered as the combination of the T_{tr}/T_a, and $2Y_{tr}/B$ parameters, and also there is high collinearity among them. Therefore, the T_{tr}/T_a, and $2Y_{tr}/B$ parameters are disregarded and instead the tr_{ratio} values are used as the first independent variable.

As can be seen in Fig. 19, there are no other independent variable that is highly correlated with k_{tr}. However, the effect of the Reynolds number on the k_{tr} was significant, as shown in Fig. 17 and must be considered. Therefore, the Reynolds number in the model scale, Re_M, was chosen as the second independent variable.

After initial attempts of regression analysis with k_{tr} and Re_M, an additional independent variable was added to capture the slight difference between low block and high block vessels, which can be seen in Fig. 14. Therefore, the longitudinal centre of buoyancy (relative to $L_{PP}/2$) was added to the regression model. The scatter plots for all independent and dependent variables are presented in Fig. 20 together with the histograms. It can be argued that a large spectrum of all three variables is covered by results from the seven hull forms in various loading conditions and Reynolds numbers.

As a result of the regression analysis, the equation below is suggested, (see Box I) where $\overline{Re_M}$ is the average of Reynolds numbers in the model scale, and the LCB is relative to $L_{PP}/2$ (in per cent of L_{PP}).

The comparison between the k_{tr} values from CFD and the empirical correction formula (Eq. (13)) is presented in Fig. 21(a). The agreement between the two prediction methods is deemed satisfactory, and the standard deviation of the residuals (subtraction of k_{tr} values from CFD and the empirical) is approximately $\sigma = 0.010$. Considering that the numerical uncertainties are 2%–3% in model and full-scale double-body RANS computations, the residuals are small enough. They somewhat resemble a normal distribution as shown in Fig. 21(b) to conclude the empirical correction formula.

The extrapolation procedure with the suggested empirical method is as follows

1. C_{TM} is obtained from the towing tank tests.
2. The model-scale form factor, k_M is determined either by the Prohaska method (Prohaska, 1966) or by model-scale CFD as described in the ITTC (2021b).
3. The residual resistance is calculated as $C_R = C_{TM} - (1 + k_M)C_{FM}$
4. The full-scale form factor, k_S, as $k_S = k_M + k_{tr}$ where
   - if $tr_{ratio} \leq 0.025$, $k_{tr} = 0$
   - if $tr_{ratio} > 0.025$, k_{tr} is calculated from the Eq. (13)
     - if the calculated $k_{tr} \leq 0$ then $k_{tr} = 0$
     - if the calculated $k_{tr} > 0$ then k_{tr} value can be used.
5. The full-scale total resistance coefficient is calculated as

$$C_{TS} = (1 + k_S)C_{FS} + \Delta C_F + C_A + C_R + C_{AAS}\ , \tag{14}$$

where,

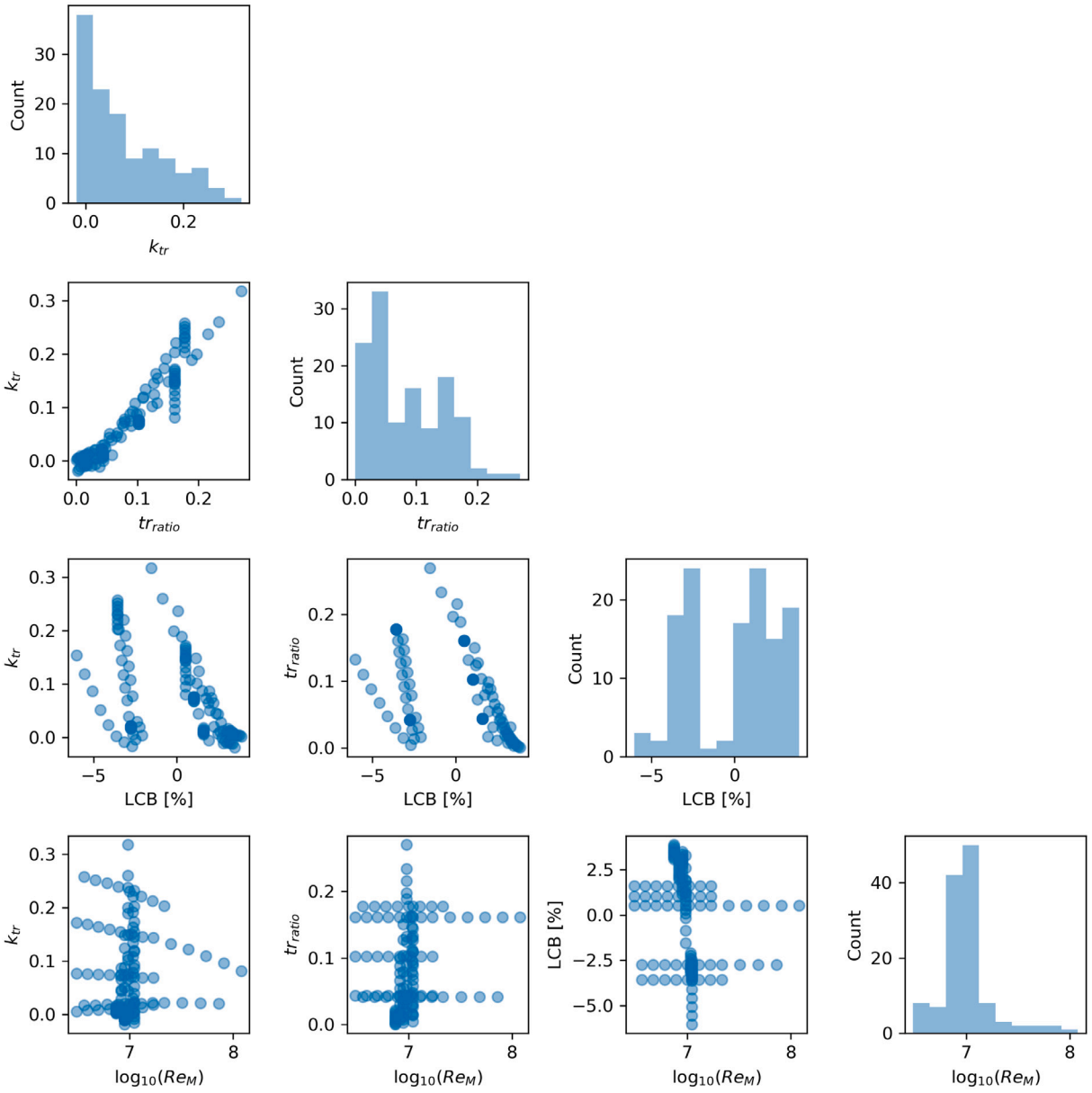

Fig. 20. Dependent and independent variables used for the regression analysis.

$$k_{tr} = \left[-0.025 + tr_{ratio}\left(1.5 - 2.3tr_{ratio} - 0.07\mathrm{LCB}\right)\right] \times \left[-5.45 + \log_{10}(\overline{Re_{\mathrm{M}}})\left(1.415 + 4.32tr_{ratio}\right) - \left(\log_{10}(\overline{Re_{\mathrm{M}}})\right)^2\left(0.081 + 0.55tr_{ratio}\right)\right] \quad (13)$$

Box I.

- Residual resistance is obtained by using the model-scale form factor
- Viscous resistance is obtained by using the full-scale form factor.

Note that the correction is proposed with a minimum transom area threshold since small tr_{ratio} values may result in partially wetted-transom or dry-transom flow. The limitation of $tr_{ratio} \leq 0.025$ approximately corresponds to $Fr_{tr} < 3.2$ for the test cases used in this study. According to Saunders (1957), the critical transom Froude number, after which the transom runs fully dry, is between 4 and 5. However, more recent studies on a 2D transom stern by Maki (1997) and Starke et al. (2007) indicated that approximately 2.5 is the critical Fr_{tr}. Thorough investigations by Doctors (2003) on the partly wetted-transom and dry transom flows resulted in a regression model which predicts the water surface drop with respect to the calm water level. Further extensive experiments by Robards and Doctors (2003) on flat-bottomed and rectangular-shaped transoms confirmed the critical Fr_{tr}

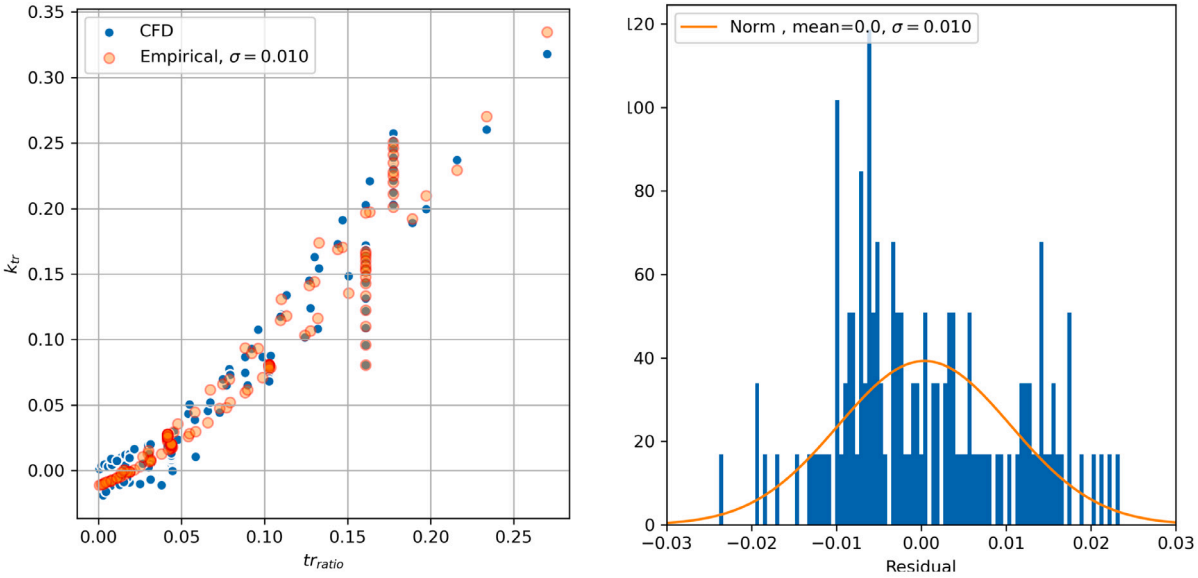

(a) k_{tr} predictions from the CFD and the empirical correction Eq 13

(b) Residuals of the regression model

Fig. 21. Local flow behind the transom of the H1 test case at scantling draught at model (left column) and full (right column) scale.

as approximately 2.5. A re-analysis of this study (Doctors, 2006) proposed an improved regression model to predict the water depreciation level behind the transom. The regression model of Robards and Doctors (2003) and Doctors (2006) were tested against the FS RANS computations presented in Section 6.2.1 to check if they could provide an accurate threshold for the empirical correction proposed in this study. The comparison of the water level predicted by the FS RANS and the regression models of Robards and Doctors (2003) and Doctors (2006) indicated opposite trends. The regression models predict that the H1 test case at the lowest draught should be almost completely in the dry-transom flow regime; however, the FS RANS computations indicate a wetted-transom (see Figs. 7 and 8). A similar observation was noted by Maki et al. (2006) where the transition of the transom flow from wet to dry for a realistic ship model was predicted prematurely by a nearly identical regression model by Doctors (2006). Based on the earlier studies, it is concluded that the prediction of the flow regime behind the transom by simple regression models is not reliable enough. The flow behind the transom depends on the overall geometry of the vessel and the wave pattern generated by the hull (Maki et al., 2006); therefore, it is recommended that the flow regime should be confirmed for small transom submergence with the help of FS RANS computations or model tests. In the case of a dry-transom or partially wetted-transom, the double-body assumptions are violated (in model or full-scale), which is a case that Eq. (13) is no longer valid regardless of the tr_{ratio} value.

7.1. Demonstration of the 2 − k method and the empirical correction procedure against the sea trials

In this study, two methods are proposed for taking into account the effects of substantial transom submergence, which is lacking in the literature and the current 1978 ITTC Performance Prediction Method (ITTC, 2021a). This section compares full-scale speed-power relations between the speed trials and full-scale predictions based on model tests. Unfortunately, due to the extreme scarcity of speed trials performed at design or scantling draughts where the transom is submerged at rest, only ten trials of sufficient quality (Werner and Gustafsson, 2020) belonging to the four hulls (H1, H2, H3, H4) could be used for the comparison.

The comparison between the speed trial measurements and the model test power predictions was performed through the correlation factors (ITTC, 2017a) used in the 1978 Performance Prediction method (ITTC, 2021a). Among three different schemes of correlation factors, C_P–C_N method was used. In this study, the correlation factor, C'_P, is calculated as

$$C'_P = \frac{P_{D\ trial}}{P_{D\ tank}} \tag{15}$$

where the $P_{D\ trial}$ is the power from a speed trial, while $P_{D\ tank}$ represents the corresponding prediction based on the model test. After individual C'_P values for each speed trial are calculated, an assembled correlation factor, C_P, is obtained by taking the median of C'_P of all trials. Due to confidentiality, the assembled correlation factors are not disclosed, but the normalised C'_P values of each prediction method are presented by shifting the median of each prediction method to 1.

The standard deviation of the normalised C'_P is considered the measure of success for different prediction methods as it was the main criterion for the determination of the original ITTC 1978 Performance Prediction Method. Considering that the precision and bias limits of a single-speed trial result amounts to nearly 10% total uncertainty as indicated by Werner and Gustafsson (2020) and Insel (2008), a meaningful reduction in scatter (standard deviation) is expected to claim an improvement confidently.

Normalised correlation factors of each hull are calculated using the same model tests results, which were extrapolated with different prediction methods,

- the standard ITTC-78 method (ITTC, 2021a) using the Prohaska method where the model and full-scale form factors are equal,
- $2 - k$ form factor method using separate CFD based form factors in model and full-scale (see Section 2),
- and the empirical correction method using Prohaska method for form factor in model scale and the corrected form factor in full scale (see Section 7).

The power predictions were made with the ITTC-57 model to ship correlation line (ITTC, 1957). In addition, the vessels with an energy-saving device ahead of the propellers were treated with a special wake scaling suggested in the ITTC 1999 method (ITTC, 1999). As explained earlier, only the calculation method of form factors in the model and full-scale differs among the three methods.

The normalised correlation factors, C'_P, are calculated for the speed trials with low to acceptable uncertainty levels, which indicates the

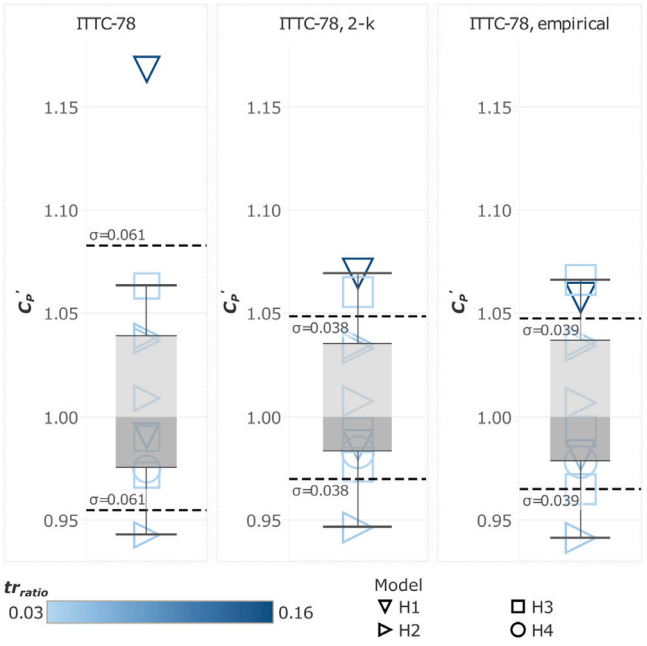

Fig. 22. Normalised correlation factors from the standard ITTC-78 method (left), CFD based $2-k$ form factor method (middle), and the empirical correction procedure (right).

trustworthiness of each speed trial by summarising the most significant error sources and weighting them according to their impact on the results. C_P' values of each prediction method are presented in Fig. 22 where the tr_{ratio} of each hull is distinguished with colour, and the different hulls are represented with different markers, the standard deviations (σ) of C_P' is presented with horizontal dashed lines, and the box plots can be identified with the grey colour, and sized with the lower and upper quartiles with the whiskers extending to the data within 1.5 times the interquartile range (IQR).

The normalised correlation factors for the standard ITTC-78 method are presented in Fig. 22 (left). It can be observed that all but the H1 hull at the scantling draught were predicted within approximately ±5%. However, the H1, which has the largest transom submergence, is greatly under-predicted by nearly 16% which is far greater than the uncertainty of a single-speed trial. According to the findings of this study, this result is expected. All hulls except the H1 at the scantling draught have relatively small transom submergence ($tr_{ratio} < 0.049$), which requires marginal corrections, i.e. the standard ITTC-78 method should mostly work well.

C_P' values from the CFD based $2-k$ form factor method is shown in Fig. 22 (middle). Compared to the predictions from the standard ITTC-78 method, the scatter (σ) was reduced from 0.061 to 0.038 when the $2-k$ form factor method was used. This reduction was largely possible thanks to the improvement in the prediction of the H1 possessing large transom submergence but also the minor improvements in all other hull forms. In order to judge the success of the $2-k$ form factor method, further analysis was performed on the size of the standard deviation. As seen in Fig. 22, two of the hulls have sister ships (different speed trials) which indicate up to 9% difference in measured power from speed trials. As discussed thoroughly in Korkmaz et al. (2021), relatively large standard deviations of C_P' are mainly due to the scatter in the speed trials of the sister ships. To demonstrate this claim, an ideal prediction condition was prepared. The ideal condition is that the mean of C_P' of a series of sisters (H2 and H3) and single trials (H1 and H4) would be 1. The standard deviation in the ideal prediction scenario yields $\sigma = 0.035$, which is very close to the scatter observed from the $2-k$ form factor method predictions.

Moving to the empirical correction procedure presented in Fig. 22 (right), the similarity of the predictions between this method and the $2-k$ method is remarkable. The scatter was effectively reduced compared to the standard ITTC-78 method; however, slightly higher than the $2-k$ form factor method. This result is somewhat expected since the form factor correction, k_{tr}, was derived from a relatively simple equation (Eq. (13)) instead of a full-scale double-body RANS computation, as is the case for the $2-k$ form factor method.

8. Conclusions

This paper investigates the wetted-transom flows often observed for the vessels with substantially submerged transoms. First, the assumptions underlying the form factor approach were discussed. Then, the shortcomings of the current 1978 ITTC Performance Prediction Method have been explained when there is a flow separation in the boundary layer surrounding the vessel. Finally, after a detailed qualitative and quantitative analysis of the wetted-transom flow, two alternative procedures were proposed to take into account the effects of the recirculating water behind the transom.

As recognised by the ITTC, the current recommended procedures of the form factor approach for any vessel with a substantial transom stern for which the transom runs wet is not valid. It is demonstrated that the form factor is not independent of the Reynolds number when there is flow separation in the boundary layer. When the same model and full-scale form factors are used to extrapolate the resistance, the full-scale viscous resistance is under-predicted in the case of a wetted-transom flow.

The two form factor method, a combined EFD/CFD method, is proposed as an alternative to the current ITTC-78 extrapolation procedure. The $2-k$ method replaces the extrapolated full-scale viscous resistance with the CFD based viscous resistance, which includes

- the form resistance that is proportional to the frictional resistance coefficient, such as the additional skin friction caused by curvature effects, flow in transverse directions, and eddy-making (typical form resistance),
- the contribution of the flow separation behind the transom that is not proportional to the frictional resistance coefficient.

Dividing the model-scale viscous pressure coefficient into two parts, $C_{PVM} = C'_{PVM} + C_{trM}$, is based on the observations on the flow features

- the shrinking of the axial velocity component, u/U, in the region outside of the wake of the transom, which indicates little to no change as the Reynolds number is increased from model to full-scale,
- the large vortex near the side of the transom close to the water surface remaining nearly the same in both scales.

This division of the form resistance is instrumental in quantifying the viscous resistance deficit emerging when the standard ITTC-78 method is used for the vessels with wetted-transom. The deficit of C_{VS} is formulated as a fraction of the frictional resistance coefficient, i.e. the transom form factor k_{tr}. It is observed that k_{tr}

- is almost exclusively correlated with the submerged area of the transom
- showed no tangible trends for the section shape of the transom ($tr_{fullness}$) or the slope of the buttocks of the stern overhang (θ)
- is highly Reynolds number dependent; hence, different model sizes may result in significantly different k_{tr} values.

The regression analysis on the transom form factor indicated that the deficit of C_{VS} can be modelled with a relatively simple equation. Therefore, an empirical correction procedure is also suggested in addition to the $2-k$ method. The empirical equation (Eq. (13)) is derived so that it can be integrated into the current 1978 ITTC Performance

Prediction Method with a simple modification of the full-scale form factor. Furthermore, the suggested empirical correction is compatible with the Prohaska method of determining the model-scale form factor and the ITTC-57 model to ship correlation line.

The power predictions from the two proposed procedures were compared to the predictions from the standard ITTC-78 method and the speed trials. The conclusions regarding the comparison of the full-scale predictions and speed trials are that:

- The precision is improved compared to the standard ITTC-78 method.
- The sample size of the validation cases is somewhat limited, but the improvement achieved by both suggested procedures is significant and in line with the theory.
- The main contributor of the standard deviation of the normalised correlation factors originates from the scatter of the speed trials among the sister ships. The standard deviation of C_P' is noticeably close to the minimum value that could be obtained (the ideal condition) from the speed trials when the $2-k$ method is used with the $k-\omega$ SST turbulence model.

In this paper, the wetted-transom flow characteristics were explained together with the shortcomings of the current ITTC Performance Prediction method, and two alternative methods were presented. The two form factor method, which combines EFD and CFD, is expected to provide immediate improvements to the power predictions of the vessels with any type of flow separation, including the wetted-transom flow due to substantial transom submergence. The empirical correction method, which requires no CFD, can be incorporated into the current ITTC-78 method as a second alternative. It can accurately restore the deficit of the extrapolated full-scale viscous resistance in the event of a wetted-transom flow. The two suggested alternative methods are expected to be instrumental in improving the accuracy and reliability of the EEDI predictions performed at the scantling draught, where the transoms of many vessels are submerged.

Further studies should be performed with more test cases, especially hulls with large transom submergence, where the speed trials are available. However, considering the extreme scarcity of sea trial data carried out at design or scantling draught where the transom is submerged at rest, free-surface RANS computations can be considered to predict full-scale conditions. As the correction required for a deeply submerged transom can be significantly large, the accuracy of state-of-the-art full-scale CFD computations may suffice to test the proposed alternative methods.

CRediT authorship contribution statement

Kadir Burak Korkmaz: Conceptualization, Methodology, Validation, Formal analysis, Investigation, Data curation, Writing – original draft preparation, Writing – review & editing, Visualization. **Sofia Werner:** Conceptualization, Methodology, Investigation, Writing - review & editing, Supervision, Project administration, Funding acquisition. **Rickard Bensow:** Conceptualization, Methodology, Investigation, Writing – review & editing, Supervision.

Declaration of competing interest

The authors declare that they have no known competing financial interests or personal relationships that could have appeared to influence the work reported in this paper.

Data availability

The data that has been used is confidential.

Acknowledgements

This research was funded by Energimyndigheten, the Swedish Energy Agency, grant 2020-018759, and the computational resources provided by SSPA Sweden AB. The authors declare no conflict of interest. The funders had no role in the design of the study; in the collection, analyses, or interpretation of data; in the writing of the manuscript, or in the decision to publish the results.

References

Broberg, L., Regnström, B., Östberg, M., 2014. SHIPFLOW Users Manual. FLOWTECH International AB, Gothenburg, Sweden.

Deng, G., Visonneau, M., 1996. Evaluation of eddy-viscosity and second-moment turbulence closures for steady flows around ships. In: 21st ONR Symposium on Naval Hydrodynamics, Trondheim, Norway. pp. 453–469.

Doctors, L.J., 2003. Hydrodynamics of the flow behind a transom stern. In: Twenty-Ninth Israel Conference on Mechanical Engineering, Technion, Haifa, Israel. p. 11.

Doctors, L.J., 2006. A numerical study of the resistance of transom-stern monohulls. In: 5th International Conference on High Performance Marine Vehicles, Sydney, Australia.

Dogrul, A., Song, S., Demirel, Y.K., 2020. Scale effect on ship resistance components and form factor. Ocean Eng. 209, 107428. http://dx.doi.org/10.1016/j.oceaneng.2020.107428, URL: http://www.sciencedirect.com/science/article/pii/S0029801820304534.

Eça, L., Hoekstra, M., 2014. A procedure for the estimation of the numerical uncertainty of CFD calculations based on grid refinement studies. J. Comput. Phys. 262, 104–130. http://dx.doi.org/10.1016/j.jcp.2014.01.006.

Farkas, A., Degiuli, N., Martic, I., 2017. Numerical simulation of the viscous flow around a tanker model. Brodogradnja 68 (2), 109–125. http://dx.doi.org/10.21278/brod68208, URL: http://hrcak.srce.hr/index.php?show=clanak&id_clanak_jezik=263572&lang=en.

Farkas, A., Degiuli, N., Martić, I., 2018. Assessment of hydrodynamic characteristics of a full-scale ship at different draughts. Ocean Eng. 156, 135–152. http://dx.doi.org/10.1016/j.oceaneng.2018.03.002, URL: https://linkinghub.elsevier.com/retrieve/pii/S0029801818302336.

García Gómez, A., 2000. On the form factor scale effect. Ocean Eng. 26, 97–109.

Hino, T., Stern, F., Larsson, L., Visonneau, M., Hirata, N., Kim, J., 2020. Numerical Ship Hydrodynamics: An Assessment of the Tokyo 2015 Workshop. Springer International Publishing, URL: https://doi.org/10.1007/978-3-030-47572-7.

Hoerner, S., 1965. Fluid-Dynamic Drag. Hoerner Fluid Dynamics, Bakersfield, California.

Hughes, G., 1954. Friction and form resistance in turbulent flow, and a proposed formulation for use in model and ship correlation. R. I. N. A. 96.

IMO, 2011. Annex 19: resolution MEPC.203(62).

Insel, M., 2008. Uncertainty in the analysis of speed and powering trials. Ocean Eng. 35 (11), 1183–1193. http://dx.doi.org/10.1016/j.oceaneng.2008.04.009, URL: http://www.sciencedirect.com/science/article/pii/S0029801808000929.

Islam, H., Guedes Soares, C., 2019. Effect of trim on container ship resistance at different ship speeds and drafts. Ocean Eng. 183, 106–115. http://dx.doi.org/10.1016/j.oceaneng.2019.03.058, URL: https://www.sciencedirect.com/science/article/pii/S0029801819301477.

ISO, 2015. Ships and marine technology – guidelines for the assessment of speed and power performance by analysis of speed trial data. 15016:2015.

ITTC, 1957. Subjects 2 and 4 skin friction and turbulence stimulation.

ITTC, 1999. Report of propulsion committee.

ITTC, 2017a. Guidelines on the determination of model-ship correlation factors. ITTC – Recommended Procedures and Guidelines 7.5-04-05-01.

ITTC, 2017b. Preparation, conduct and analysis of speed/power trials. ITTC – Recommended Procedures and Guidelines 7.5-04-01-01.

ITTC, 2021a. 1978 ITTC performance prediction method. ITTC – Recommended Procedures and Guidelines 7.5-02-03-01.4.

ITTC, 2021b. Practical guidelines for ship resistance CFD. ITTC – Recommended Procedures and Guidelines 7.5–03–02–04.

ITTC, 2021c. Quality assurance in ship CFD application. ITTC – Recommended Procedures and Guidelines 7.5–03-01–02.

ITTC, 2021d. Quality assurance in ship CFD application. ITTC – Recommended Procedures and Guidelines 7.5-03-01-02.

ITTC, 2021e. Resistance test. ITTC – Recommended Procedures and Guidelines 7.5-02-02-01.

Katsui, T., Asai, H., Himeno, Y., Tahara, Y., 2005. The proposal of a new friction line. In: Fifth Osaka Colloquium on Advanced CFD Applications to Ship Flow and Hull Form Design, Osaka, Japan.

Korkmaz, K.B., Werner, S., Bensow, R., 2019a. Investigations for CFD based form factor methods. In: Numerical Towing Tank Symposium (NuTTS 2019).

Korkmaz, K.B., Werner, S., Bensow, R., 2019b. Numerical friction lines for CFD based form factor determination method. In: VIII International Conference on Computational Methods in Marine Engineering MARINE 2019.

Korkmaz, K.B., Werner, S., Bensow, R., 2021. Verification and validation of CFD based form factors as a combined CFD/EFD method. J. Mar. Sci. Eng. 9 (1), http://dx.doi.org/10.3390/jmse9010075, URL: https://www.mdpi.com/2077-1312/9/1/75.

Korkmaz, K.B., Werner, S., Sakamoto, N., Queutey, P., Deng, G., Yuling, G., Guoxiang, D., Maki, K., Ye, H., Akinturk, A., Sayeed, T., Hino, T., Zhao, F., Tezdogan, T., Demirel, Y.K., Bensow, R., 2020. CFD based form factor determination method. Ocean Eng..

Larsson, L., Raven, H.C., 2010. Ship Resistance and Flow. The Society of Naval Architects and Marine Engineers, Jersey City, New Jersey.

Larsson, L., Stern, F., Visonneau, M., 2014. Numerical Ship Hydrodynamics: An Assessment of the Gothenburg 2010 Workshop. Springer, URL: https://doi.org/10.1007/978-94-007-7189-5.

Maki, K.J., 1997. Transom Stern Hydrodynamics (Doctoral dissertation). Naval Architecture and Marine Engineering, University of Michigan, Michigan.

Maki, K., Doctors, L., Beck, R., Troesch, A., 2006. Transom-stern flow for high-speed craft. Aust. J. Mech. Eng. 3, 191–199. http://dx.doi.org/10.1080/14484846.2006.11464508.

Menter, F.R., 1994. Two-equation eddy-viscosity turbulence models for engineering applications. AIAA J. 32 (8), 1598–1605. http://dx.doi.org/10.2514/3.12149, arXiv:https://doi.org/10.2514/3.12149.

NMRI, 2015. Tokyo 2015 a workshop on CFD in ship hydrodynamics. URL: http://www.t2015.nmri.go.jp/.

Orych, M., Larsson, L., 2015. Hydrodynamic aspects of transom optimization. In: 5th High Performance Yacht Design Conference, Auckland, New Zealand. pp. 247–256.

Orych, M., Werner, S., Larsson, L., 2021. Validation of full-scale delivered power CFD simulations. Ocean Eng. 238, 109654. http://dx.doi.org/10.1016/j.oceaneng.2021.109654, URL: https://linkinghub.elsevier.com/retrieve/pii/S0029801821010301.

Pereira, F.S., Eça, L., Vaz, G., 2017. Verification and validation exercises for the flow around the KVLCC2 tanker at model and full-scale Reynolds numbers. Ocean Eng. 129, 133–148, URL: https://doi.org/10.1016/j.oceaneng.2016.11.005.

Prohaska, C.W., 1966. A simple method for the evaluation of the form factor and low speed wave resistance. In: Proceeding of 11th ITTC.

Raven, H.C., van der Ploeg, A., Starke, A.R., Eça, L., 2008. Towards a CFD-based prediction of ship performance - progress in predicting full-scale resistance and scale effects. Int. J. Marit. Eng. Trans. R. Inst. Naval Archit. A.

Regnström, B., 2008. Introduction to Overlapping Grids in SHIPFLOW. FLOWTECH International AB, Gothenburg, Sweden.

Robards, S.W., Doctors, L.J., 2003. Transom hollow prediction for high-speed displacement vessels. In: International Conference on Fast Sea Transportation, Ischia, Italy. pp. A1.19–A1.26.

Saunders, H. (Ed.), 1957. Hydrodynamics in Ship Design, Vol. 2. Society of Naval Architects and Marine Engineers, pp. 529–531.

SIMMAN, 2008. SIMMAN 2008 workshop verification and validation of ship manoeuvring simulation methods. http://www.simman2008.dk/KVLCC/KVLCC2/kvlcc2_geometry.html.

Starke, B., Raven, H., van der Ploeg, A., 2007. Computation of transom-stern flows using a steady free-surface fitting RANS method. In: 9th International Conference on Numerical Ship Hydrodynamics. p. 18.

Terziev, M., Tezdogan, T., Incecik, A., 2019. A geosim analysis of ship resistance decomposition and scale effects with the aid of CFD. Appl. Ocean Res. 92, URL: https://doi.org/10.1016/j.apor.2019.101930.

Toki, N., 2008. Investigation on correlation lines through the analyses of geosim model test results. J. Japan Soc. Naval Archit. Ocean Eng. 8, 71–79.

Tokyo, 2015. Tokyo 2015 a workshop on CFD in ship hydrodynamics. https://t2015.nmri.go.jp/kcs.html.

Wang, Z.Z., Xiong, Y., Shi, L.P., Liu, H., 2015. A numerical flat plate friction line and its application. J. Hydrodyn. 23, 383–393.

Werner, S., Gustafsson, L., 2020. Uncertainty of speed trials. In: HullPIC 2020, Rotterdam, Holland.